
THE KORI–ULB ICE FLOW MODEL

REFERENCE MANUAL



FRANK PATTYN

Contributors: K. Bulthuis, V. Coulon, E. Kazmierczak, S. Sun, L. Zipf

Laboratoire de Glaciologie, Université libre de Bruxelles,

Avenue F.D. Roosevelt 50, B-1050 Brussels, Belgium (Frank.Pattyn@ulb.be)

Kori–ULB v1.0 — April 27, 2023



kori (*noun*):

1. ice (Japanese)
2. movement (Maori)

TERMS AND CONDITIONS

The Kori-ULB Ice Flow Model is a 2.5-dimensional finite difference numerical ice sheet model of intermediate complexity.

MIT License

Copyright (c) 2023 Frank Pattyn

Permission is hereby granted, free of charge, to any person obtaining a copy of this software and associated documentation files (the "Software"), to deal in the Software without restriction, including without limitation the rights to use, copy, modify, merge, publish, distribute, sublicense, and/or sell copies of the Software, and to permit persons to whom the Software is furnished to do so, subject to the following conditions:

The above copyright notice and this permission notice shall be included in all copies or substantial portions of the Software.

THE SOFTWARE IS PROVIDED "AS IS", WITHOUT WARRANTY OF ANY KIND, EXPRESS OR IMPLIED, INCLUDING BUT NOT LIMITED TO THE WARRANTIES OF MERCHANTABILITY, FITNESS FOR A PARTICULAR PURPOSE AND NONINFRINGEMENT. IN NO EVENT SHALL THE AUTHORS OR COPYRIGHT HOLDERS BE LIABLE FOR ANY CLAIM, DAMAGES OR OTHER LIABILITY, WHETHER IN AN ACTION OF CONTRACT, TORT OR OTHERWISE, ARISING FROM, OUT OF OR IN CONNECTION WITH THE SOFTWARE OR THE USE OR OTHER DEALINGS IN THE SOFTWARE.

Copyright © 2023 Frank Pattyn (Frank.Pattyn@ulb.be)

Contents

1	Introduction	6
2	Model basics	8
2.1	Overview	8
2.2	Field equations	8
2.2.1	Mass conservation	9
2.2.2	Momentum balance	10
2.2.3	Conservation of energy	10
2.2.4	Constitutive equations and the equation of motion	10
3	Model call	12
3.1	Requirements	12
3.2	Model run	12
3.3	Mandatory control parameters	12
3.4	Optional control parameters	13
3.5	Example: Rectangular isothermal ice sheet	14
4	Input and output data	16
4.1	Input file: <code>infile</code>	16
4.2	Output file: <code>outfile</code>	17
4.3	Parameter file: <code>KoriInputParams.m</code>	17
5	Ice velocities	22
5.1	Approximations	22
5.2	Shallow-Ice Approximation (SIA)	22
5.3	HySSA approximation	22
5.4	Control parameters for velocity	23
6	Ice temperature and rheology	24
6.1	Ice temperature	24
6.2	Thermomechanical coupling	25
6.3	Control parameters for thermodynamics	25
6.4	Example: Rectangular thermo-coupled ice sheet	26
7	Basal sliding and subglacial conditions	28
7.1	Regularized Coulomb friction law	28
7.2	Effective pressure at the ice sheet base	29
7.2.1	Height above buoyancy	29
7.2.2	Subglacial water film	30
7.2.3	Sliding related to water flux	31
7.2.4	Effective pressure in till	31
7.3	Control parameters for basal sliding and hydrology	32

8	Calving, hydrofracturing and sub-shelf pinning	33
8.1	Preamble	33
8.2	Description	33
8.3	Control parameters for calving	35
9	Glacial Isostatic Adjustment (GIA)	36
9.1	Bedrock deformation for a plate with constant thickness	36
9.2	Plate with constant thickness on a viscous substratum	37
9.3	Plate with spatially-varying thickness	38
9.4	Time-dependent bedrock response	38
9.5	Geoid changes	39
9.6	Control parameters for GIA	39
10	Grounding-line flux condition for power-law sliding	40
10.1	Description	40
10.2	Control parameters for grounding-line flux	41
11	Model initialization	42
11.1	Methodology	42
11.2	Control parameters for optimization	43
12	Datasets for initialization and forcing	44
12.1	Datasets for the Antarctic ice sheet	44
13	Atmospheric forcing	45
14	Ocean forcing	49
14.1	The PICO ocean-coupler model	49
14.2	PICOP and plume model	50
14.3	Non-local melt-rate parametrization (ISMIP6)	52
	References	54

1 Introduction

Kori–ULB is an ice flow model applicable to ice sheets and glaciers on Earth (both land-terminating and marine ice sheets), as well as ice masses on other planets (such as the Martian North Pole Layered Deposits). It reduces the three-dimensional nature of ice sheet flow and its dynamics to a two-dimensional problem, while keeping the essential characteristics of ice sheet and ice stream flow. Kori–ULB is the follow-up of f.ETISh (fast Elementary Thermomechanical Ice Sheet model; Pattyn, 2017). While f.ETISh was essentially designed for large-scale simulations of the Antarctic ice sheet (Pattyn, 2017; Bulthuis et al., 2019; Coulon et al., 2021), it has been extended to high-resolution simulations of glacier flow, specific drainage basins of ice sheets and specific ice geometries, such as MISIP3d, MISIP+ and Thule.

Compared to the initial version of f.ETISh (Pattyn, 2017), several improvements have been made and extensions have been implemented, the most important are listed below:

1. To facilitate the integration of the Earth-system model output with ice sheet models, several sub-shelf melt models have been implemented, such as PICO (Potsdam Ice-shelf Cavity mOdel; Reese et al., 2018a) that links far-field ocean temperature and salinity to sub-shelf melting via a box model of overturning circulation within ice-shelf cavities (Olbers and Hellmer, 2010). Furthermore, the plume parametrization (Lazeroms et al., 2018) has been implemented as well as its combination with PICO, called PICOP (Pelle et al., 2019).
2. Kori–ULB can easily be forced with atmospheric and oceanic output from General Circulation Models as used in ISMIP6 (Seroussi et al., 2020; Edwards et al., 2021). Coupling with atmosphere and ocean models has been done recently (Pelletier et al., 2021).
3. Basal sliding has been significantly improved through the implementation of a general sliding law, based on regularized Coulomb friction (Gagliardini et al., 2007; Joughin et al., 2019; Zoet and Iverson, 2020). This allows to control a higher plasticity of the fast-flowing outlet glaciers, while keeping a power-law relationship (Weertman-type sliding law) for slower-moving ice.
4. Subglacial hydrology has been implemented through subglacial water flow based on a thin water film and a porous water model in subglacial till.
5. Calving and hydrofracturing results in a dynamic boundary for floating ice shelves in contact with the ocean.
6. Changes in the geoid due to mass changes of ice sheets have are now taken into account, leading to non-uniform sea level changes that may impact grounding-line stability. The standard bedrock adjustment based on an elastic lithosphere and relaxed asthenosphere (ELRA-model) has been extended to spatially varying characteristics of both lithosphere effective thickness and mantle viscosity (Coulon et al., 2021).
7. Ice sheet model initialization has been improved with a two-step method, allowing to optimize basal melt rates underneath ice shelves, akin to optimizing basal sliding coefficients, to keep the ice sheet in steady-state (Bernales et al., 2017).

Some ongoing developments are:

1. Implementation of the Level Set Function (LSF) for the calving boundary of ice shelves and cliffs.
2. Ice shelf damage (Sun et al., 2017).

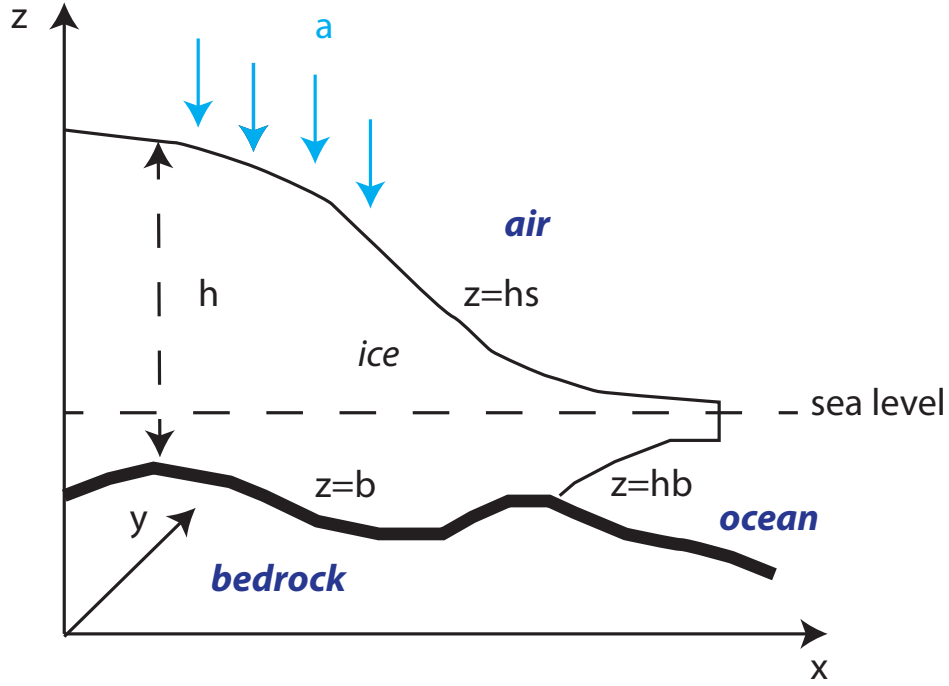


Figure 1: General Cartesian geometry of the Kori–ULB model.

2 Model basics

2.1 Overview

The Kori–ULB model consists of diagnostic equations for ice velocities, and three prognostic equations for the temporal evolution of ice thickness, ice temperature, and bedrock deformation beneath the ice. Prescribed boundary fields are equilibrium bedrock topography, basal sliding coefficients, geothermal heat flux, and sea level. Present-day mean surface air temperatures and precipitation are derived from data assimilation within climate models. Optionally, ablation is determined from a Positive Degree-Day model and sub-shelf melt through simplified ocean circulation models. The Cartesian geometry used is given in Fig. 1. For the coupled ice sheet/ice shelf system the surface elevation h_s is defined as

$$h_s = \max \left[b + h, \left(1 - \frac{\rho_i}{\rho_s} \right) h + z_{sl} \right], \quad (1)$$

where h is the ice thickness, b is the bedrock elevation, z_{sl} is the sea-level height with respect to the chosen datum, ρ_i and ρ_s are the ice and seawater density, respectively. It follows that the bottom of the ice sheet equals $h_b = h_s - h$, and that $h_b = b$ holds for the grounded ice sheet.

2.2 Field equations

The Stokes equations then approximate the Navier-Stokes equations for fluid flow, by neglecting momentum advection and inertia terms. Despite these approximations, the flow of ice is in a sense more complicated than the flow of air or water because it is not a Newtonian

fluid. In other words, there is a non-linear relationship between the applied stress and the resulting strain rates. Deriving the Stokes equations requires a series of equations that relate conservation laws to the mechanical and thermal properties of the material. These are the conservation of mass, momentum and energy, known as the field equations. In order to link them, they are substituted into the field equations to obtain a system of numerically solvable equations, which is demonstrated below.

2.2.1 Mass conservation

Conservation of mass is described by the continuity equation,

$$\frac{d\rho_i}{dt} + \nabla \cdot (\mathbf{v}\rho_i) = 0 \quad (2)$$

where \mathbf{v} is the velocity vector. Considering ice as an incompressible material ($\rho_i = \text{constant}$), this can be reduced to the incompressibility condition,

$$\nabla \cdot \mathbf{v} = 0 \quad (3)$$

where $\mathbf{v} = (u, v, w)$ are the velocity components in (x, y, z) and from which it follows that

$$w(s) - w(b) = - \int_b^s \nabla \cdot \mathbf{v}_H(z) dz \quad (4)$$

where \mathbf{v}_H are the components of the horizontal velocity (u, v) . At the upper and lower surfaces, respectively, kinematic boundary conditions apply, i.e.,

$$w(b) = \frac{\partial b}{\partial t} + \mathbf{v}_H(b) \cdot \nabla b - M \quad (5)$$

$$w(s) = \frac{\partial h_s}{\partial t} + \mathbf{v}_H(h_s) \cdot \nabla h_s - \dot{a} \quad (6)$$

where \dot{a} (positive in case of accumulation) and M (positive in case of melt) are the surface and basal mass balance, respectively. Using the Leibniz integration rule, the combination with the kinematic boundary conditions leads to

$$\frac{\partial h}{\partial t} = -\nabla \cdot (\mathbf{v}_H h) + \dot{a} - M \quad (7)$$

For the specific case of calculating ice velocities with the Shallow-ice approximation (SIA), Eq. (7) is written as a diffusion equation, i.e.,

$$\frac{\partial h}{\partial t} = \nabla \cdot (d \nabla h_s) + \dot{a} - M, \quad (8)$$

where d are diffusion coefficients for the velocity defined as

$$d = -\frac{2}{n+2} A h^{n+2} (\rho_i g)^n |\nabla h_s|^{n-1} - u_b h (\nabla h_s)^{-1} \quad (9)$$

and where h_b is the bottom of the ice sheet (or the bedrock elevation b for the grounded ice sheet) and where d contains both the deformational u_d and sliding u_b contributions (Huybrechts, 1992).

2.2.2 Momentum balance

Conservation of linear momentum is defined as:

$$\rho_i \frac{d\mathbf{v}}{dt} = \nabla \cdot \boldsymbol{\sigma} - \rho_i \mathbf{g} \quad (10)$$

where $\boldsymbol{\sigma}$ is the Cauchy stress tensor and $|\mathbf{g}| = 9.81 \text{ m s}^{-2}$ is the gravitational acceleration. For an ice sheet, the acceleration term (left hand side of 10) and the Coriolis force can be safely neglected. For a constant ice density, the momentum balance can be rewritten as

$$\nabla \cdot \boldsymbol{\sigma} + \rho_i \mathbf{g} = 0 \quad (11)$$

The conservation of angular momentum ensures that the Cauchy tensor is symmetric, i.e. $\boldsymbol{\sigma} - \boldsymbol{\sigma}^T = 0$, where $\boldsymbol{\sigma}^T$ is the transpose of $\boldsymbol{\sigma}$.

2.2.3 Conservation of energy

The final field equation is conservation of energy, which solves the thermodynamics of the ice, i.e.,

$$\rho_i c_p \frac{\partial T}{\partial t} = \nabla \cdot (K \nabla T) - \rho_i c_p \mathbf{v} \cdot \nabla T + 2\dot{\boldsymbol{\epsilon}} \cdot \boldsymbol{\sigma} \quad (12)$$

where K is the thermal conductivity of ice, c_p is the heat capacity of ice, and T is the ice temperature.

2.2.4 Constitutive equations and the equation of motion

In order to solve the field equations, a constitutive equation is required, which is the material law equation that relates stress to strain. Glacier ice is a polycrystalline fluid with a stress-dependent viscosity. Due to its structure, there is a non-linear relationship between the applied stress and the resulting deformation, which can be expressed through Glen's flow law. Stress and deformation rates (represented by the strain tensor $\dot{\boldsymbol{\epsilon}}$) are assumed to follow a power law with a proportionality factor that depends on the ice rheology, which in turn depends on local ice temperature, i.e.,

$$\dot{\boldsymbol{\epsilon}} = A \sigma_e^{n-1} \boldsymbol{\tau} \quad (13)$$

where $\boldsymbol{\tau}$ is the deviatoric stress tensor, which are those stresses remaining once the hydrostatic stresses $p\mathbf{I}$ are removed from $\boldsymbol{\sigma}$,

$$\boldsymbol{\tau} = \boldsymbol{\sigma} + p\mathbf{I} \quad (14)$$

where

$$p = -\frac{1}{3} \text{tr} \boldsymbol{\sigma} \quad (15)$$

Since ice is considered incompressible, deformation does not depend on the total stress, but the deviation from the isotropic pressure p (defined positive when compressed). σ_e is the effective stress, defined as the second invariant of the stress tensor $\boldsymbol{\sigma}$ and defined by

(making use of the Einstein summation convention) $\sigma_e^2 = \frac{1}{2} \sum \tau_{ij} \tau_{ji}$, or written in terms of tensor components,

$$2\sigma_e^2 = \tau_{xx}^2 + \tau_{yy}^2 + \tau_{zz}^2 + 2(\tau_{xy}^2 + \tau_{xz}^2 + \tau_{yz}^2) \quad (16)$$

A is the temperature-dependent rate factor that obeys an Arrhenius law and may vary over several orders of magnitude within an ice sheet. This is the reason why modelling large ice sheets requires thermomechanical coupling and solving conservation of energy. For simplicity, rather than accuracy, we will continue with a constant value for A . The power law exponent n is generally assigned a value of 3. For application of this flow relation in the momentum equation, it is required that $\boldsymbol{\tau}$ is a function of $\dot{\boldsymbol{\epsilon}}$. For this purpose, the inverse of Glen’s flow law is used,

$$\boldsymbol{\tau} = 2\eta\dot{\boldsymbol{\epsilon}} \quad (17)$$

where η is the effective viscosity of the ice, which is strain-dependent due to the non-linear nature of the flow law,

$$\eta = \frac{1}{2} A^{-1/n} \dot{\epsilon}_e^{(1-n)/n} \quad (18)$$

where $\dot{\epsilon}_e$ is the effective strain rate, defined as the second invariant of $\dot{\boldsymbol{\epsilon}}$, i.e., $\dot{\epsilon}^2 = \frac{1}{2} \sum \dot{\epsilon}_{ij} \dot{\epsilon}_{ji}$. The components of $\dot{\boldsymbol{\epsilon}}$ are defined as,

$$\dot{\epsilon}_{ij} = \frac{1}{2} \left(\frac{\partial v_i}{\partial x_j} + \frac{\partial v_j}{\partial x_i} \right) \quad (19)$$

Substituting (17) into the simplified momentum balance equation (11), results in the equation of motion,

$$-\nabla p + \nabla \cdot \left[\eta \left(\nabla \mathbf{v} + (\nabla \mathbf{v})^T \right) \right] + \rho_i \mathbf{g} = 0 \quad (20)$$

In Kori–ULB, the the Stokes equations (20) are approximated by the shallow-ice and shallow-shelf equations, which is detailed in Section 5.

3 Model call

3.1 Requirements

The Kori-ULB model is built in MATLAB[®] and makes use of standard MATLAB[®] toolboxes. Required toolboxes are MATLAB[®], Signal Processing Toolbox, Image Processing Toolbox, and Statistics and Machine Learning Toolbox. The model runs with versions of MATLAB[®] R2016b onwards.

3.2 Model run

Kori-ULB is based on two MATLAB[®] script files, i.e., `KoriModel.m` containing the main model code and subroutines and `KoriInputParams.m` containing the main input parameters and constants, excluding parameters that control the model. A further script is needed that creates a MATLAB[®] file with all controlling variables to call `KoriModel.m`. The Kori-ULB model is called with the following command line in MATLAB[®]:

```
KoriModel(infile,outfile,ctr);
```

or

```
KoriModel(infile,outfile,ctr,fc);
```

where `ctr` is a 1×1 struct containing values and settings of parameters that control the model run, `fc` is a 1×1 struct with fields containing time-dependent forcing control of the model, `infile.mat` is the input file with either the observed ice sheet geometry or the results of a previous model run. The output file `outfile.mat` is similar to the input file in structure and saves all required matrices to produce a follow-up run. Finally, a variable dump file is automatically created after each model run containing all variables of the model run. This file is named `outfile_toto.mat`. Note that `infile.mat` does not need to exist (it should be defined though). In that case, all initial field values will be set to default values. Also, `fc` is an optional file that by default is set to zero (no forcing).

3.3 Mandatory control parameters

The control file is a MATLAB[®] (.mat) file listing all control parameters necessary to run the model. It can be created with a simple script. Most parameters are set to their default values and should not explicitly be defined. One particularity of the input files is the definition of (x, y) corresponding to (j, i) in the numerical code. In other words, the first element of a matrix corresponds to its vertical position, the second element to its horizontal one. It suffices to transpose input data sets to make the visualization of data fully compliant.

ctr.dt : time step (years).

ctr.imax : number of grid points in the y -direction.

ctr.jmax : number of grid points in the x -direction.

ctr.delta : grid size (m), equal in both x and y -directions.

ctr.nsteps : number of iterations in time, so that $(nsteps - 1) \times dt = \text{total model run time in years}$.

3.4 Optional control parameters

Optional control parameters define the output of the model, how and whether plots are made, and define what domain is considered (full ice sheet, basin, or synthetic experiments).

ctr.diagnostic :

0 : Normal model run (default);

1 : Run model without ice-thickness evolution (all other model components run normally).

ctr.basin : Solution of a specific drainage basin. In that case, **MASK** = -1 for the grounded areas outside the drainage basin (the entire model domain remains rectangular). Default=0. [See section on basins.](#)

ctr.mismip : Synthetic experiments on a rectangular domain with specific boundary conditions. Default=0. [See section on MISMIP.](#)

ctr.plotH : Output in standard plot changes in ice thickness (default), surface elevation (**ctr.plotH** = 1), or ice thickness (**ctr.plotH** = 2). Default=0.

ctr.plotGL :

1 : Plot grounding line in output graphs, when grounding line exists (default);

0 : No grounding line plotting.

ctr.restart :

0 : Normal model run (default);

1 : Restart from latest dump file (when **ctr.runmode**=1 or **ctr.runmode**=3).

ctr.runmode :

0 : Run model with graphics that are shown every **ctr.snapshot** (default). A dump file is written at the end of the model run. The name of the dump file is **outfile_toto.mat**;

1 : Run model with graphics and output dump is written every **ctr.snapshot**. This allows for restarting the model after failure;

2 : As in 0 but run without graphics (especially useful when using batch jobs)

3 : As in 1 but run without graphics (especially useful when using batch jobs and securing recovery);

ctr.snapshot : number of snapshots in time dependency and graphical output; for grounding-line monitoring when **ctr.timeslice**=1, snapshot should preferentially be smaller than 250, since it may increase the number of output files dramatically (limit = 999). Default value = 100.

ctr.starttime : Define start time of model run in years. Default=0.

ctr.timeslice :

- 0** : no extra output (default);
- 1** : will provide extra output for forcing experiments saved sequentially in a file (snapshot times). The variable list is defined by `par.varlist` and consists of a list of 2-d matrices to be saved in each file.

3.5 Example: Rectangular isothermal ice sheet

This example is probably the simplest setup of running an ice sheet model. We consider an isothermal ice sheet on a square flat bedrock, forced by a constant surface mass balance, starting from zero ice thickness. Ice deformation is according the shallow-ice approximation (SIA). The script is given below:

```
% EISMINT fixed margin experiment for an isothermal ice sheet

ctr.imax=31;
ctr.jmax=31;
ctr.delta=50.e3;
ctr.nsteps=501;
ctr.dt=50.;

Mb=zeros(ctr.imax,ctr.jmax)+0.3;
save('SIMPLE','Mb');

KoriModel('SIMPLE','simple_out',ctr);
```

Basic input is the number of elements in x and y , the spatial resolution Δ (m), the number of iterations and the time step Δt (a). Additional information is given in the input file, where the surface mass balance M_b (m a^{-1}) is defined as a matrix of the size of the domain. Output will be written in two files, i.e., `simple_out.mat` and `simple_out_toto.mat`. The latter contains all the variables (dump file) at the end of the model run, while the former contains essential matrix information that is used as input for a follow-up run. Thanks to the exhaustive use of default values for parameters, only a limited amount of data needs to be defined to run a model in its simplest way.

Besides the creation of both files at the end of the model run, graphic information will be displayed during the run (default), which is shown in Figures 2 and 3.

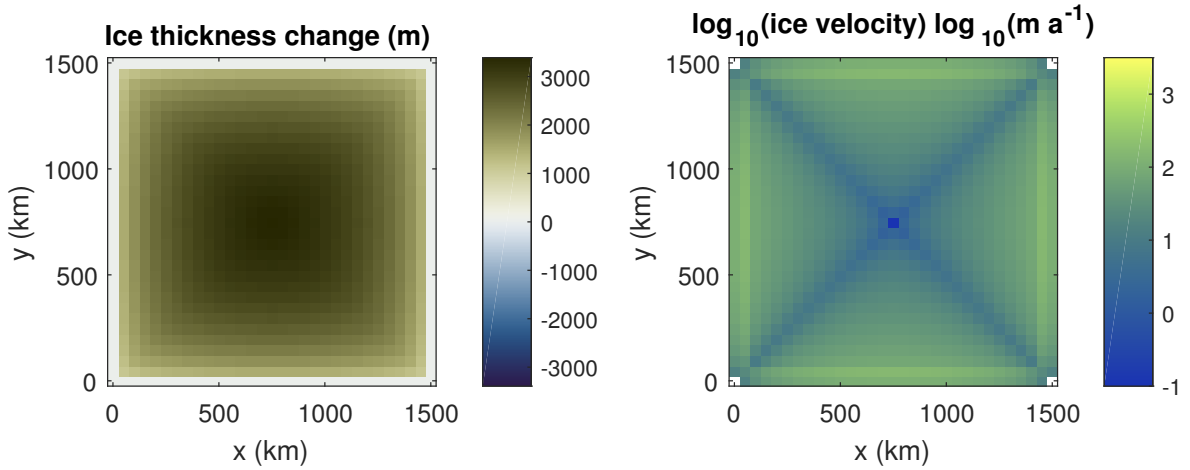


Figure 2: Basic output figure of the simple rectangular ice sheet model. The left panel shows the change in ice thickness (starting from zero thickness). The right panel displays a logarithmic plot of the ice velocities.

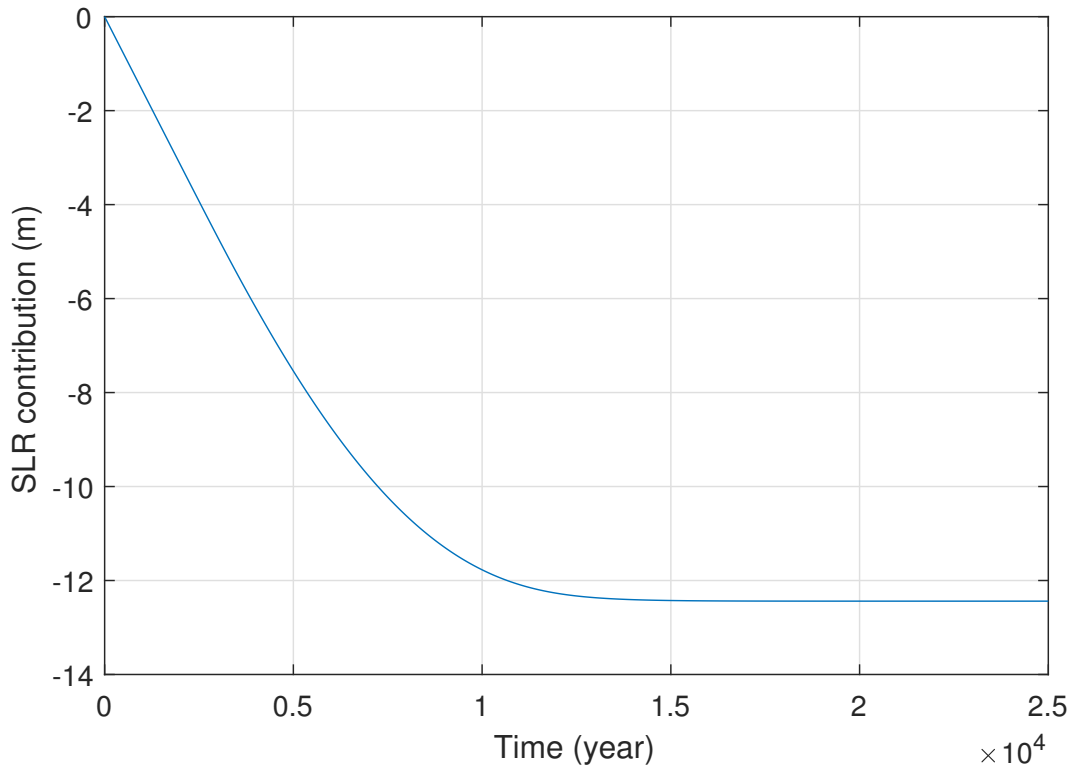


Figure 3: Basic output figure at the end of the model run displaying the ice volume change (above floatation) in terms of sea level contribution as a function of time.

4 Input and output data

4.1 Input file: **infile**

infile is the name of a .mat input file with following (optional) 2d variables that can be compiled separately: **MASK**, **MASKo**, **H**, **Ho**, **B**, **Bo**, **Bor**, **G**, **stdB**, **Ts**, **Mb**, **Pr**, **Evp**, **To**, **So**, **Db**, **Btau**, **v**, **vx**, **vy**, **lat**, **lon**, **ZB**, where

MASK : grounded = 1; floating = 0

Note that when **shelf=0** and **schoof=0**, the model domain will be restricted to **MASK=1**

MASKo : observed **MASK** (invariable in time) and corresponding to **MASK** prior to any simulation.

H : ice thickness (m)

Ho : observed ice thickness (m), invariable in time

B : bedrock elevation (m)

Bo : observed bedrock elevation (m), invariable in time. Note that on the borders of the domain, for Antarctic and Greenland configurations, *B* is set to -4000 m to prevent grounding lines to move outside the domain.

Bor : original observed bedrock elevation (m), invariable in time (not altered as in **Bo**).

G : geothermal heat flux (W m^{-2})

stdB : Standard deviation of bedrock variability within a grid cell (based on original Bedmap2 or BedMachine data).

Ts : Annual mean surface temperature ($^{\circ}\text{C}$). Note that this is the unforced value (observed).

Mb : Surface mass balance (m a^{-1}).

Pr : Precipitation (m a^{-1}). This variable will be used when the PDD model for calculating surface melt is used, not **Mb**.

Evp : Evaporation (m a^{-1}). Used in conjunction with **Pr**.

To : Ocean temperatures on the continental shelf ($^{\circ}\text{C}$).

So : Ocean salinity on the continental shelf (PSU).

Db : Flexural rigidity of the lithosphere.

Btau : Relaxation time of the asthenosphere (filled with constant values corresponding to **bedrelax** when **Btau** is not initially defined).

v : observed surface velocity *v*.

vx : observed surface velocity *v* in *x* (on staggered *u*-grid)

vx : observed surface velocity v in y (on staggered v -grid)

lat : Latitude (degrees)

lon : Longitude (degrees)

ZB : Delineation of drainage basins.

Note that the name of the input file should be given, but the file itself should not necessarily exist. If the file is non-existent, the model will be initialized with zero matrices of H , B , As , $stdB$, Ts , Mb , and tmp . $MASK$ will be set to 1 everywhere, and G will contain a constant value of geothermal heat flow of $G=0.042 \text{ W m}^{-2}$. The extension '.mat' should not be given as part of the name `infile`.

4.2 Output file: outfile

`outfile` is the name of a .mat output file (same structure as `input`). This file will contain all necessary matrices to be used as an input file for a subsequent experiment. During successive runs, more input will be added, such as `Bmelt`, `As`, `Asor`, `tmp`, `uxssa`, `uyssa`, `Wd`, `Wtil`, `Meltinv`. These variables are produced by the model and used for successive model runs.

All model data and parameters are stored in a file with the name `outfile_toto.mat`. The extension '.mat' should not be given as part of the name `infile`. For `ctr.snapshot=1`, file names starting from `outfile_000.mat` with an increment of 1 will be created where variables listed in `par.varlist` will be saved.

4.3 Parameter file: KoriInputParams.m

All major parameters and constants are stored in the file `KoriInputParams.m`. They are listed below.

```
%-----  
% General control parameters  
%-----  
  
par.dcolor='broc'; % Crameri colorscale  
par.color='imola'; % Crameri colorscale  
  
%-----  
% Numerical control parameters  
%-----  
  
par.maxspeed=40e3; % maximum ice speed limit (m/a)  
par.omega=2.5; % Crank-Nicolson scale factor  
               % (0=explicit; 1=implicit; >1 over-implicit)  
par.secpereyear=31556926;  
% 2d variables to be saved when timeslice=1  
par.varlist={'MASK', 'H', 'B', 'ux', 'uy', 'flux', 'Tbc', 'SLR', 'Neff', 'Melt'};  
  
%-----  
% Subglacial characteristics  
%-----
```

```
par.PoreFrac=0.96; % Fraction of water pressure to balance ice pressure
par.longcoupwater=5; % distance in number of ice thicknesses over which
    % hydraulic gradient coupling takes place
par.dirpp_war=[9 8 7 6 5 4 3 2 1];
par.waterviscosity=1.8e-3/par.secperyear;
par.NeffScale=5e6; % scale factor for Effective Pressure
par.Wdmin=1e-8; % minimum value for Wd and Wtil
par.Wdmax=0.015; % maximum value for Wd
par.Wmax=2; % maximum value for Wtil (2 m)
par.flw0=1e5; % maximum value for subglacial water flux
par.Cdr=1e-3; % background till drainage rate
par.Cc=0.12; % till compressibility (Tulaczyk et al., 2000a)
par.e0=0.69; % reference void ratio at N0 (Tulaczyk et al., 2000a)
par.N0=1e3; % reference effective pressure (Tulaczyk et al., 2000a)
par.sigmat=0.02; % Ntil lower bound, as fraction of overburden pressure

%-----
% Ice dynamics
%-----

par.ShelfPinning=1; % sub-shelf pinning of ice shelves
par.g=9.81; % gravitational acceleration
par.rho=917.; % ice density
par.rhow=1027.; % sea water density
par.rhom=3370.; % lithosphere density
par.n=3; % flow law exponent
par.visciter=50; % max number of iterations over effective viscosity
    % in SSA solution
par.visctol=5e-1; % limit for iterations over effective viscosity
    % in SSA solution
par.veliter=50; % max iteration number for iterative SSA velocity solver
par.veltol=1e-4; %VL: tolerance for iterative SSA velocity solver
if basin==1
    par.veltol=par.veltol/10;
end
par.Hiter=20; %VL: max iteration number for iterative thickness solver
par.Htol=1e-6; %VL: tolerance for iterative thickness solver
par.Z=2*(par.g*par.rho)^par.n; % SIA isothermal pre-term
par.dlim=0.5; % Limit on local crevasses depth (% of H)
par.damlim=0.9; % limit on total damage (% of H)

%-----
% Ice-ocean interactions
%-----

par.Latent=3.35e5; % Latent heat of freezing
par.cp0=3974.; % Heat capacity of ocean water
par.Soi=34.5; % ocean salinity for initialization
par.Toi=-1.7; % Ocean temperature for initialization
par.SeaIceThickness=0.1;
par.ArcOcean=0; % include Ocean Arc to control Melt and calving
par.LatentMelt=(par.rhow*par.cp0)/(par.rho*par.Latent);

%-----
% PICO and plume model parameters
```

```
%-----
par.nbox=5; % max number of ocean boxes
par.alphao=7.5e-5;
par.betao=7.7e-4;
par.rhoref=1033;

par.lambda1=-5.73e-2;
par.lambda2=8.32e-2;
par.lambda3=7.61e-4;
par.gamma0=1.447733676e4;
par.gamma1=0.545;
par.gamma2=3.5e-5;
par.CdGamT=1.1e-3;
par.CdGamTS0=6e-4;
par.Eo=3.6e-2;
par.Cd=2.5e-3;
par.x0=0.56;

% Melt function coefficients (Lazeroms)
par.pcof=[0.1371330075095435
  5.527656234709359e1
 -8.951812433987858e2
  8.927093637594877e3
 -5.563863123811898e4
  2.218596970948727e5
 -5.820015295669482e5
  1.015475347943186e6
 -1.166290429178556e6
  8.466870335320488e5
 -3.520598035764990e5
  6.387953795485420e4];

% Plume V2 constants (Lazeroms 2019)
par.C_eps_lazero = 0.6; % Slope correction parameter
par.alpha_coeff_lazero = 3.87e-5; % degC-1 Thermal expansion coefficient
par.beta_coeff_lazero = 7.86e-4; % psu-1 Haline contraction coefficient

%-----
% Isostasy
%-----

par.FlexRigid=1e25; % Flexural rigidity
par.bedrelax=3000.; % relaxation time astenosphere
par.nuB=0.25; % Poisson ratio in flexural rigidity

%-----
% Local sea level (fingerprints)
%-----

par.Re=6.3781e6; % Radius Earth
par.Me=5.972e24; % Mass Earth
par.Aoc=3.618e14; % ocean surface
par.geoidist=5000e3; % size of convolution filter
par.rhof=1000; % fresh water density
```

```
par.Slref=0; % reference sea level

%-----
% Model initialization
%-----

par.stdDevRegul=3.5; % standard deviation of the Gaussian filter for
                    % the regularization in grid cells (3.5)
if basin==1
    par.stdDevRegul=par.stdDevRegul+1;
end
par.invmin=1.e-10; % values valid for m=2; scaled with 150kPa for other m
par.invmax=1.e-3;
par.invmaxncor=1.e-5;
par.AsFroz=1e-11;
par.AsScale=1e5^(2-m);

%-----
% Thermodynamics
%-----

par.T0=273.15; % absolute temperature
par.K=2.1; % thermal conductivity
par.kdif=1.1487e-6; % kdif=K/(rho*cp), cp=2009; value of EISMINT
par.pmp=8.66e-4; % Clausius Clapeyron (Payne, 2000)
par.atune=1; % tuning factor in Arrhenius (1 for n=3; 1e-5 for n=4)
par.R=8.314; % gas constant
par.udfrac=0.25;
par.intT=10; % number of iterations for which tmp is calculated
par.TrTemp=-10; % Basal temperature for which ice is frozen to bed
par.Q1=78.2e3; % Arrhenius parameters from Ritz (1992)
par.Q2=95.45e3;
par.a1=1.66e-16;
par.a2=2e-16;

%-----
% PDD model parameters
%-----

par.PDDth=0; % PDD threshold temperature (0C)
par.Train=2;
par.Tsnow=0;
par.snowfac=3/par.rho; % PDD factor for snow melt
par.icefac=8/par.rho; % PDD factor for ice melt
par.d_ice=5; % Maximum depth of refreezing of percolating meltwater (m)
par.Tlapse=-0.008; % Lapse rate for temperature correction with height
par.Tsigma=4; % standard dev of mean T for PDD calculation
par.Psigma=3.5; % standard dev of mean T for rain factor calculation
par.PDDsteps=48;

%-----
% Basin model parameters
%-----
```

```
par.As0=1e-20; % sliding coefficient outside basin  
par.A0=1e-20; % Ice fluidity outside basin
```

5 Ice velocities

5.1 Approximations

The ice sheet model has several modes of operation, depending on the boundary conditions that are applied. The most elementary flow regime of the grounded ice sheet is according to the Shallow-Ice approximation (SIA; Hutter, 1983), extended with a Weertman-type (or regularized Coulomb friction) law for basal sliding. A more appropriate mode of operation for most applications is the hybrid mode, in which the flow regime of the grounded ice sheet is governed by a combination of SIA, responsible for ice-deformational flow, and the Shallow-Shelf approximation (SSA; Morland, 1987; MacAyeal, 1989) for basal sliding, which exerts a given friction at the ice sheet base (Bueler and Brown, 2009; Martin et al., 2011; Winkelmann et al., 2011). Ice shelf flow is governed by the SSA, defined by zero basal drag and extended by a water-pressure condition at the seaward edge.

5.2 Shallow-Ice Approximation (SIA)

The Shallow-Ice approximation (SIA; Hutter, 1983) is commonly used in ice sheet modelling. This approximation is valid for ice sheets of small aspect ratios $h \ll L$, where L is the horizontal length scale of the ice sheet domain, and further characterized by a low curvature and low sliding velocities. The approximation is, however, not valid near grounding lines nor for ice shelf flow, for which other approximations are applied (see below). According to SIA, the vertical mean horizontal velocity in an ice sheet is given by

$$\mathbf{v}_{\text{SIA}} = \mathbf{v}_b + \frac{2A}{n+2} h |\tau_d|^{n-1} \tau_d, \quad (21)$$

where $\tau_d = -\rho_i g h \nabla h_s$ is the driving stress, $\mathbf{v}_b = (u_b, v_b)$ is the basal sliding velocity and $\mathbf{v}_{\text{SIA}} = (u, v)$ is the vertical mean horizontal velocity according to SIA.

5.3 Hybrid Shallow-Shelf/Shallow-Ice approximation (HySSA)

The flow velocity in an ice shelf or an ice stream characterized by low drag is derived from the Stokes equations (Stokes, 1845) by neglecting vertical shear terms and by integrating the force balance over the vertical (Morland, 1987; MacAyeal, 1989). The hybrid (HySSA) model considers that inland ice flow is governed by both deformational velocity (represented by Eq. (21)) and membrane stresses incorporated in basal sliding $\mathbf{v}_b = \mathbf{v}_{\text{SSA}}$. Bueler and Brown (2009) use a weighing function to ensure a continuous solution of the velocity from the interior of the ice sheet across the grounding line to the ice shelf. However, Winkelmann et al. (2011) have demonstrated that a simple addition (for the grounded ice sheet velocities) still guarantees a smooth transition for ice-stream flow, i.e., $\mathbf{v} = \mathbf{v}_{\text{SIA}} + \mathbf{v}_{\text{SSA}}$. Here, we incorporate both into one equation, which leads to the following set of equations for both horizontal components of the ice velocity $\mathbf{v} = (u, v)$,

$$2 \frac{\partial}{\partial x} \left(2\eta h \frac{\partial u}{\partial x} + \eta h \frac{\partial v}{\partial y} \right) + \frac{\partial}{\partial y} \left(\eta h \frac{\partial u}{\partial y} + \eta h \frac{\partial v}{\partial x} \right) - \beta^2 u = -\tau_{dx} - \beta^2 u_{\text{SIA}}, \quad (22)$$

$$2 \frac{\partial}{\partial y} \left(2\eta h \frac{\partial v}{\partial y} + \eta h \frac{\partial u}{\partial x} \right) + \frac{\partial}{\partial x} \left(\eta h \frac{\partial v}{\partial x} + \eta h \frac{\partial u}{\partial y} \right) - \beta^2 v = -\tau_{dy} - \beta^2 v_{\text{SIA}}, \quad (23)$$

where

$$\eta = \frac{A^{-1/n}}{2} \left[\left(\frac{\partial u}{\partial x} \right)^2 + \left(\frac{\partial v}{\partial y} \right)^2 + \frac{\partial u}{\partial x} \frac{\partial v}{\partial y} + \frac{1}{4} \left(\frac{\partial u}{\partial y} + \frac{\partial v}{\partial x} \right)^2 + \varepsilon_0^2 \right]^{(1-n)/2n}, \quad (24)$$

and where $\tau_{dx} = \rho_i g h (\partial h_s / \partial x)$ (similar for τ_{dy}), and by definition $\tau_{bx} = \beta^2 u$ (similar for τ_{by}). $\varepsilon_0 = 10^{-20} \text{ a}^{-1}$ is a small factor to keep η finite, hence to prevent singularities when velocity gradients are zero. For the ice shelf, $\beta^2 = 0$. The SSA stress-equilibrium equations (22) and (23) require boundary conditions to be specified along the contour which defines the boundary to the ice-shelf domain, which is taken as the edge of the computational domain, irrespective of whether or not calving is considered. Dynamic conditions (specification of stress) are applied at this seaward edge, so that the vertically-integrated pressure balance then reads

$$2\eta h \left[\left(2 \frac{\partial u}{\partial x} + \frac{\partial v}{\partial y} \right) n_x + \frac{1}{2} \left(\frac{\partial u}{\partial y} + \frac{\partial v}{\partial x} \right) n_y \right] = n_x \frac{1}{2} \rho_i g h^2 \left(1 - \frac{\rho_i}{\rho_s} \right), \quad (25)$$

$$2\eta h \left[\left(2 \frac{\partial v}{\partial y} + \frac{\partial u}{\partial x} \right) n_y + \frac{1}{2} \left(\frac{\partial u}{\partial y} + \frac{\partial v}{\partial x} \right) n_x \right] = n_y \frac{1}{2} \rho_i g h^2 \left(1 - \frac{\rho_i}{\rho_s} \right), \quad (26)$$

where n_x, n_y are the outward-pointing normal vectors in the x and y direction, respectively. These boundary conditions are applied at the edges of the domain, or to specific domain boundaries only when `ctr.mismip` > 0.

5.4 Control parameters for velocity

ctr.SSA :

- 0** : SIA solution for grounded ice sheet (default);
- 1** : calculation of SSA for grounded ice sheet and ice shelf
- 2** : calculation of the hybrid HySSA model (SSA+SIA) for the grounded ice sheet.

ctr.shelf :

- 0** : no ice shelves (default);
- 1** : add ice shelves (requires that `ctr.SSA` > 0).

ctr.upstream :

- 1** : Upstream differences for ice velocities u, v in advection part of the ice-thickness equation (default). Does not apply to the SIA model.
- 0** : Central differences

ctr.BetaIter : Number of iterations on β^2 calculation in the nonlinear part of the SSA velocity calculations (default); can be set throughout to `ctr.nsteps`. Default = 5.

ctr.ItSolv : Iterative solver for both the ice thickness and the SSA/HySSA velocities (default=1).

6 Ice temperature and rheology

6.1 Ice temperature

The diffusion–advection equation for an ice sheet (and ice shelf) is given by (Huybrechts, 1992):

$$\frac{\partial T}{\partial t} = \kappa \frac{\partial^2 T}{\partial z^2} - u \frac{\partial T}{\partial x} - v \frac{\partial T}{\partial y} - w \frac{\partial T}{\partial z} + \frac{\Phi_d}{\rho_i c_p}, \quad (27)$$

where $\kappa = K/\rho_i c_p$ is the thermal diffusivity of ice, K is the thermal conductivity, c_p is the heat capacity of ice, T is the ice temperature, and $\Phi_d = -\rho_i g (h_s - z) \nabla h_s \partial \mathbf{v}_d / \partial z$ represents deformational heating, where \mathbf{v}_d is the deformational velocity component ($\mathbf{v}_d = \mathbf{v} - \mathbf{v}_b$). The basal boundary condition is given by

$$\frac{\partial T_b}{\partial z} = \frac{G + \tau_d \mathbf{v}_b}{K}, \quad (28)$$

where G is the geothermal heat flux and the second term represents frictional heating at the base. The last term in Eq. (28) represents strain heating. Phase changes at the base are incorporated in the model by keeping the basal temperature at the pressure melting point whenever it is reached or basal melt water is present. The basal melt rate \dot{b} (positive when melting) is calculated from the difference between the basal temperature gradient in Eq. (28) and the gradient corrected for pressure melting,

$$\dot{b} = \frac{K}{\rho L} \left[\left(\frac{\partial T_b}{\partial z} \right)_c - \frac{G + \tau_d \mathbf{v}_b}{K} \right] \quad (29)$$

where the subscript c denotes the gradient corrected for pressure melting, and L is the specific latent heat for fusion. Given the two-dimensional nature of the model, the temperature field employs shape functions for vertical profiles of deformational velocity \vec{v}_d , its vertical gradient, and the vertical velocity, based on SIA (Hindmarsh, 1999). Eq. 27 is then solved in scaled vertical coordinates $\zeta = (h_s - z)/h$, with $\zeta = 0$ at the surface and $\zeta = 1$ at the bottom of the ice sheet. The use of shape functions for horizontal and vertical velocities allows for a faster calculation of the thermodynamic model. We follow the approach by Lliboutry (1979) and Ritz (1992) that take into account a higher power of the horizontal velocity profile due to softer ice at the bed, hence higher shear strain rates, i.e.,

$$\mathbf{v} = \frac{\dot{\gamma}_b h}{p_r + 2} \quad (30)$$

where

$$\dot{\gamma}_b = B_0 \tau_d^n \exp \left[\frac{Q}{R} \left(\frac{1}{T_{mb}} - \frac{1}{T_b} \right) \right] \quad (31)$$

and

$$p_r = n - 1 + \frac{Q G h}{R T_b^2} \quad (32)$$

so that,

$$\mathbf{v}(\zeta) = \mathbf{v}_b + \frac{p_r + 2}{p_r + 1} (1 - \zeta^{p_r+1}) \mathbf{v} \quad (33)$$

and following Pattyn (2010),

$$w(\zeta) = -\dot{a} \left(1 - \frac{p_r + 2}{p_r + 1} (1 - \zeta) + \frac{1}{p_r + 1} (1 - \zeta)^{p_r+2} \right) - m + \mathbf{v} \nabla b + (1 - \zeta) \mathbf{v} \nabla h \quad (34)$$

For an isothermal ice sheet, $p_r = n$.

6.2 Thermomechanical coupling

The flow parameter A and its temperature dependence on temperature are specified as in Ritz (1987, 1992):

$$\begin{aligned} A &= \frac{1}{2} E_f 1.66 \times 10^{-16} \exp \left[\frac{78.20 \times 10^3}{R} \left(\frac{1}{T_m} - \frac{1}{T^*} \right) \right] \\ &\quad \text{if } T^* \geq 266.65\text{K} \\ A &= \frac{1}{2} E_f 2 \times 10^{-16} \exp \left[\frac{95.45 \times 10^3}{R} \left(\frac{1}{T_m} - \frac{1}{T^*} \right) \right] \\ &\quad \text{if } T^* < 266.65\text{K}, \end{aligned} \quad (35)$$

where $T^* = T - T_m$ is the homologous temperature, with $T_m = -8.66 \times 10^{-4} (1 - \zeta) h$ the pressure melting correction and R the gas constant. Units of A are $\text{Pa}^{-3} \text{yr}^{-1}$ corresponding to $n = 3$. The enhancement factor E_f is set to 1 for the main ice sheet model, and to $E_f = 0.5$ for ice shelves. The ratio of enhancement factors represent differences in fabric anisotropy between grounded and ice shelf ice (Ma et al., 2010).

6.3 Control parameters for thermodynamics

ctr.Tcalc :

- 0** : No temperature calculation (default)
- 1** : Calculate temperature field in ice sheet (and ice shelf), isothermal ice sheet ($A = A_o$)
- 2** : Calculate temperature field and thermomechanical coupling, , i.e. $A = f(T)$

ctr.Tinit :

- 0** : Initial temperature field read from input file or when not available kept constant at values of surface temperature (default);
- 1** : Initialization of temperature field from semi-analytical steady-state temperature solution;
- 2** : Always use the steady-state semi-analytical solution.

ctr.Ao : Isothermal value of Glen's flow law parameter A ($\text{Pa}^{-n} \text{a}^{-1}$); Default = 10^{-16} .

ctr.shelftune : Tuning factor for the ice shelf to take into account anisotropy (Ma et al., 2010). Lower values make ice shelf more viscous. Defined as matrix so that different values can be attributed to different ice shelves. Default = 0.5.

ctr.kmax : number of vertical layers for temperature calculation (default = 11).

6.4 Example: Rectangular thermo-coupled ice sheet

Using the same simple setup as before, we will consider a thermomechanically-coupled ice sheet on a square flat bedrock, forced by a constant surface mass balance. Ice deformation is according the shallow-ice approximation (SIA). The script looks the following:

```
% EISMINT fixed margin experiment for a thermo-coupled ice sheet

ctr.imax=31;
ctr.jmax=31;
ctr.delta=50.e3;
ctr.nsteps=1001;
ctr.dt=50.;
ctr.Tcalc=2;
ctr.kmax=21;

Mb=zeros(ctr.imax,ctr.jmax)+0.3;
Ts=zeros(ctr.imax,ctr.jmax)-35;
save('SIMPLE','Mb','Ts');

KoriModel('SIMPLE','simple_out',ctr);
```

Output of the temperature field along the central axis of the domain and the horizontal velocity field along the same axis and according to (33) are displayed in Figs. 4 and 5, respectively.

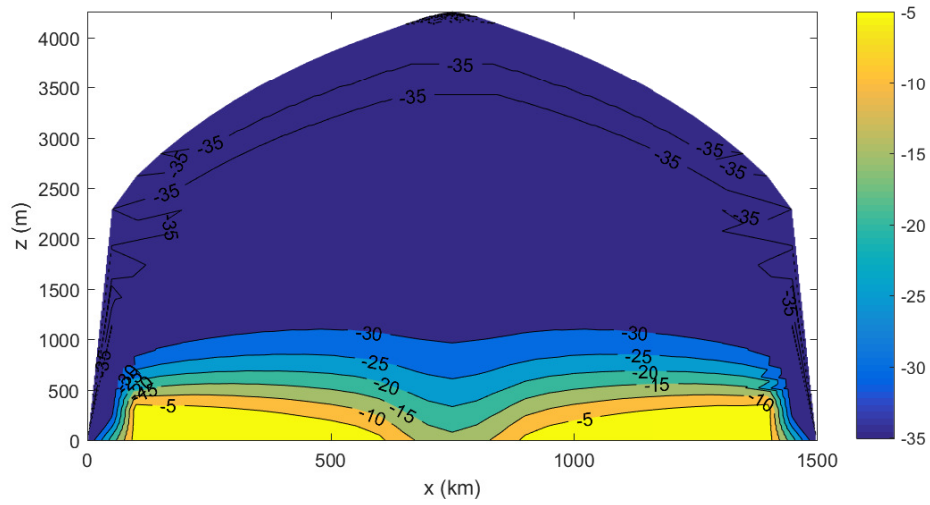


Figure 4: Englacial temperature distribution along the central flowline of the rectangular domain.

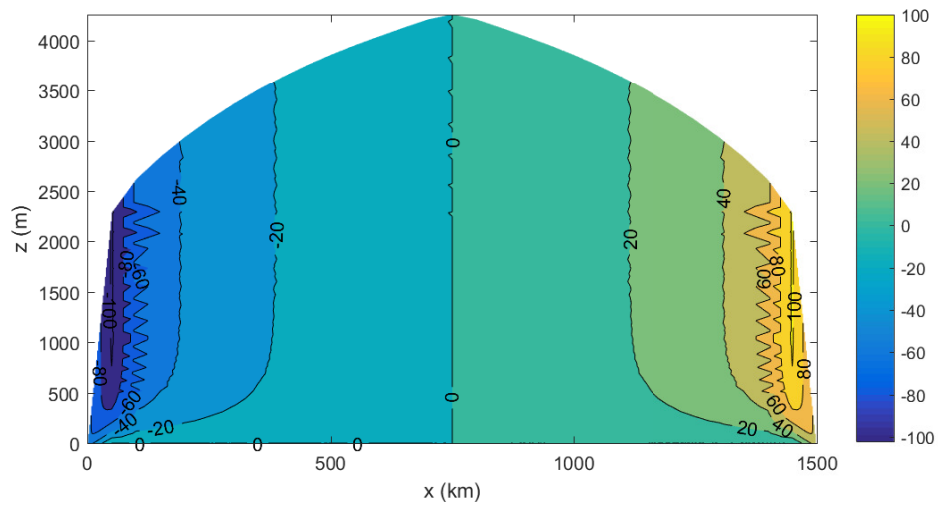


Figure 5: Horizontal velocities along the central flowline of the rectangular domain. **Wiggles are due to the poor contouring algorithm – need something better.**

7 Basal sliding and subglacial conditions

7.1 Regularized Coulomb friction law

We use a generalized slip law, or regularized Coulomb friction law, that reconciles both Weertman/Budd and Coulomb slip laws (Schoof, 2005; Gagliardini et al., 2007; Joughin et al., 2019; Zoet and Iverson, 2020; Helanow et al., 2021):

$$\tau_b = CN \left(\frac{|\mathbf{v}_b|}{|\mathbf{v}_b| + u_0} \right)^{1/m} \frac{\mathbf{v}_b}{|\mathbf{v}_b|} = CN \left(\frac{|\mathbf{v}_b|}{|\mathbf{v}_b| + A'_b C^m N^m} \right)^{1/m} \frac{\mathbf{v}_b}{|\mathbf{v}_b|} \quad (36)$$

where, $A'_b = u_0(CN)^{-m}$ is a sliding coefficient, often used when a friction law is written as a sliding law. Low speeds and high effective stresses result in viscous Weertman-style sliding; high sliding speeds and low effective stresses – conditions commonly present at the bases of ice streams – promote shallow deformation of the bed at its Coulomb strength. The main advantage of this description is that the transition from power-law slip to plastic Coulomb occurs smoothly.

In the Kori–ULB model, we formulate the slip law as a function of $f(A'_b, u_0)$, instead of $f(C, u_0)$ in Joughin et al. (2019) or $f(A'_b, C)$ in Helanow et al. (2021). Since $A'_b = u_0(CN)^{-m}$, we can write Eq. (36) as

$$\tau_b = A'^{-1/m}_b \left(\frac{u_0}{|\mathbf{v}_b| + u_0} \right)^{1/m} |\mathbf{v}_b|^{1/m-1} \mathbf{v}_b \quad (37)$$

where the term between brackets varies between 0 (plastic) and 1 (viscous). This general slip law can be related to other existing laws by:

- Budd law: $u_0 \gg |\mathbf{v}_b|$,
- Weertman law: $u_0 \gg |\mathbf{v}_b|$ and N is a constant value,
- Plastic Coulomb: $u_0 \approx 0$, so that $\tau_b \approx CN$.

Through the definition of $A'_b = u_0(CN)^{-m}$, the general slip law can in principle be expressed as a sliding law so that it fits in with the SIA description, i.e.,

$$\mathbf{v}_b = \frac{1}{\alpha} A'_b |\tau_d|^{m-1} \tau_d \quad (38)$$

where

$$\alpha = 1 - \frac{A'_b}{u_0} |\tau_d|^m \quad (39)$$

Note that the limiting condition is that $0 < \alpha \leq 1$. This means that the sliding law can never be pure plastic ($\alpha = 0$), but comes very close to plasticity for high sliding velocities. For $\alpha = 1$, the sliding law takes the form of the Budd/Weertman sliding law and corresponds to $u_0 \rightarrow +\infty$. The basal sliding factor A'_b implicitly incorporates u_0 , is a function of the effective pressure N and is also temperature dependent. The latter allows for sliding within a basal temperature range between -3 and 0°C . It further takes into account sub-grid sliding across mountainous terrain (Pollard et al., 2015):

$$A'_b = N^{-p} [(1 - r)A_{\text{froz}} + rA_b] , \quad (40)$$

where $r = \max[0, \min[1, (T^* - T_r)/(-T_r)]]$, A_{froz} is the sliding coefficient in case of frozen bedrock (chosen to be very small but different from zero to avoid singularities in the basal friction calculation), T^* is the temperature corrected for the dependence on pressure (see Section 6.2) and $T_r = \min[-3 - 0.02\sigma_b]$, where σ_b is the standard deviation of bedrock elevation within the grid cell (Pollard et al., 2015). Basal sliding factors A_b are either considered constant in space/time or are spatially varying and obtained through optimization methods (see Sect. 11). The exponent p equals m of the sliding law when effective pressure is calculated, and takes the value $p = 0$ otherwise.

Finally, the value for the basal sliding coefficient `ctr.Asin` is a nominal value for $m = 2$ and automatically scaled for other values of m through a scaling factor that is multiplied with A_b

$$A_{\text{scale}} = 10^{5(2-m)} \quad (41)$$

This way, the value of `ctr.Asin` can be kept more or less the same for different choices of m (see also Section 11). A typical value for `ctr.Asin` is $A_b = 3 \times 10^{-9} \text{ m a}^{-1} \text{ Pa}^{-2}$ for the Antarctic ice sheet, corresponding to $m = 2$ and is decreased with 10^5 for each increase of m by one unit.

7.2 Effective pressure at the ice sheet base

There are different ways of representing the effective pressure at the base of an ice sheet generally done in ice sheet models. In theory, the effective pressure N represents the ice overburden pressure p_o , i.e., the downward force due to the weight of overlying ice and till, minus the subglacial water pressure (p_w):

$$N = p_o - p_w = \rho_i g h - p_w \quad (42)$$

In the following sections, we describe in more detail on how either subglacial water pressure p_w or effective pressure N is determined.

7.2.1 Height above buoyancy

Subglacial water pressure is often neglected in ice sheet models and therefore its relationship with the effective pressure and the basal sliding is often neglected too. A simple way is to link p_w to the depth of the bed below sea level. Near grounding lines in direct contact with the ocean, subglacial water pressure of saturated till may be approximated by (Tsai et al., 2015):

$$p_w = -P_w \rho_s g (b - z_{sl}) , \quad (43)$$

where P_w is a fixed fraction of the overburden pressure. Eq. (43) is valid for $b - z_{sl} < 0$, otherwise $p_w = 0$. By definition, $p_w = \rho_i g h$ at the grounding line and underneath floating ice shelves, so that the effective pressure becomes zero (or close to zero when modulated by the value of P_w). This means that only marine terminated parts of the ice sheet are impacted by the subglacial water. According to Lüthi et al. (2002), the pore water pressure, i.e., the

pressure of the subglacial water mixed with the solid part of the till, represents a fraction slightly smaller than 100% of the ice overburden pressure. Bueler and Brown (2009) consider the pore water pressure locally as at most a fixed fraction ($P_w = 95\%$) of the ice overburden pressure $\rho_i gh$. The fraction varies among different studies, i.e., 96% (Winkelmann et al., 2011), 97% (Van Pelt and Oerlemans, 2012), and 99% (Gandy et al., 2019). This is probably the most common representation of subglacial water pressure in large-scale Antarctic ice sheet models.

7.2.2 Subglacial water film

Subglacial water flow can be introduced following the method of Le Brocq et al. (2009) based on a single element type to describe the morphology of the drainage system, i.e., a Weertman-type water film (Flowers, 2015). The model assumes that water flows in a thin film of water of the order of 10^{-3} m thickness. The evolution of the water film depth d_w is given by

$$\frac{\partial d_w}{\partial t} = M - \nabla \cdot (\mathbf{u}_w d_w) \quad (44)$$

where M is the basal melt rate (positive for melting) underneath the grounded ice sheet, and \mathbf{u}_w is the depth-averaged water film velocity, calculated using a theoretical treatment of laminar flow between two parallel plates, driven by differences in the water pressure (Weertman, 1966):

$$\mathbf{u}_w = \frac{d_w^2}{12\mu} \nabla \Phi \quad (45)$$

where μ is the viscosity of water and Φ is the hydraulic potential. The hydraulic potential represents the total mechanical energy per unit volume of water required to move the water from one state to another (Flowers, 2015), and is a function of the elevation potential and the water pressure, i.e.,

$$\Phi = \rho_w gb + p_w = \rho_w gb + \rho_i gh - N \quad (46)$$

The water pressure, p_w , is a function of the ice overburden pressure and the effective pressure N . In a distributed system, however, the water pressure will be close to, if not at, the overburden pressure. As a result, a simplification can be made to Eq. (46), assuming N to be zero (see, e.g., Budd and Jenssen, 1987; Alley, 1996). The assumption that N is zero simplifies the calculation of the hydraulic potential surface by removing the need to calculate the water pressure. With this simplification, the gradient of the potential surface is written as

$$\nabla \Phi = \rho_i g \nabla h_s + (\rho_w - \rho_i) g \nabla b \quad (47)$$

Taking $\partial d_w / \partial t = 0$ in Eq. (44) (steady-state approach), it is possible to use a flux balance approach to calculate the steady-state water depth (in a similar way to balance velocity calculations; see, e.g., Budd and Warner (1996) or Le Brocq and others (2006), for more details). The balance approach requires the outgoing flux in any given grid cell to be equal to the incoming water flux plus the local melt rate within the cell. The routing direction of the subglacial water is given by the hydraulic potential gradient $\nabla \Phi$. The water depth is then obtained from the outgoing water flux Q_l , i.e.,

$$d_w = \left(\frac{12\mu Q_l}{|\nabla\Phi|} \right)^{\frac{1}{3}} \quad (48)$$

Subglacial water thickness is then related to subglacial water pressure through

$$p_w = P_w \rho g h \left(\frac{d_w}{d_w^0} \right), \quad (49)$$

where $d_w^0 = 0.0015$ m is a limit value to the subglacial water thickness.

7.2.3 Sliding related to water flux

Alternatively, Goeller et al. (2013) propose to introduce a simple physically plausible correlation of the sliding rate factor and the subglacial water flux:

$$A_b = A_o \exp \left(\frac{\Phi}{\Phi_0} \right), \quad (50)$$

where Φ_0 is a limit factor on the subglacial water flux, taken as 10^5 (Goeller et al., 2013), and A_o the initial value of A_b . A similar approach has been followed by Pattyn et al. (2005). The approach is rather intuitive than physical and just considers that basal sliding increases when the water flux beneath the ice sheet increases.

7.2.4 Effective pressure in till

Bueler and Brown (2009) employ an effective thickness of stored liquid water at the base of the ice column. This layer of thickness W is used to estimate the subglacial water pressure reduced to the pore water pressure according to

$$p_w = P_w \rho_i g h \frac{W}{W_{\max}}, \quad (51)$$

where W_{\max} is the maximum saturated till thickness, fixed at 2 m, which has an impact on the till weakening by pressurized water. A fixed fraction of ice overburden equal to one will imply that the yield stress becomes zero in the case of full till saturation (Van Pelt and Oerlemans, 2012). An alternative way, which has been used here, to derive the effective pressure in the case of a deformable bed composed by a permeable till is to express the effective pressure, N , in Eq. (42) as a function of the sediment void ratio, e , due to the changing water content in the till (van der Wel et al., 2013; Bougamont et al., 2014), i.e.,

$$N = N_0 \times 10^{-(e-e_0)/C_c}, \quad (52)$$

where e_0 is the void ratio at a reference effective pressure N_0 and C_c is the till compressibility. Bueler and van Pelt (2015) propose to employ Eq. (52) in a hydrological model of subglacial water drainage within an active layer of the till, W . As the water in till pore spaces is much less mobile than that in the linked-cavity system because of the very low hydraulic conductivity of till, an evolution equation for W_{til} without horizontal transport can be written (Bueler and van Pelt, 2015)

$$\frac{\partial W}{\partial t} = M - C_t \quad (53)$$

Here C_t is a fixed rate that makes the till gradually drain in the absence of water input; we choose C_t to be 1 mm a^{-1} , which is small compared to typical values of subglacial melt. We constrain the layer thickness by

$$0 \leq W \leq W_{\max} \quad (54)$$

The effective pressure N is then written as the following function of W (Bueler and van Pelt, 2015),

$$N = N_0 \left(\frac{\delta P_o}{N_0} \right)^s 10^{(\frac{e_0}{c_c})(1-s)} \quad (55)$$

where $s = W/W_{\max}$ and bounded by $N = \min \{p_o, N\}$ and δp_o is the lower bound on N , taken as a fraction of the ice overburden pressure.

7.3 Control parameters for basal sliding and hydrology

ctr.m : Power sliding law exponent according to Weertman sliding law (default = 1).

ctr.u0 : Value of u_0 in the regularized Coulomb friction law. Large values (default) indicate Weertman-type sliding. (default=1e12)

ctr.p : Exponent for effective pressure in Weertman sliding law (default = 0).

ctr.Asin : Matrix of size (ctr.imax,ctr.jmax) with coefficients of sliding parameters A_b prior to initialization. Will be overwritten if **As** is already defined in the **infile**.

ctr.SlidAdjust :

0 : Basal sliding based on coefficients A_s , either constant value or optimized field (default);

1 : As above, but basal sliding is also a function of basal temperature (within a range of **par.TrTemp** °C from the local pressure melting point) and bedrock variability **stdB** to allow for sliding in mountainous areas (only when **stdB** exists; this is also invoked in the inversion procedure).

ctr.subwaterflow :

0 : no subglacial hydrology, i.e., water pressure calculated from depth of the bed below sea level (default);

1 : runs the subglacial water flow model (subglacial hydrology) and calculates effective pressure based on subglacial water thickness;

2 : Porous till water model (Bueler and van Pelt, 2015);

3 : Subglacial hydrology model of Goeller et al. (2013).

8 Calving, hydrofracturing and sub-shelf pinning

8.1 Preamble

This section will be further improved in future, as brittle processes will be introduced with an improved physical representation. These processes will not only include calving and hydrofracturing, but damage of ice sheets and ice shelves as well.

8.2 Description

Ice-front calving is obtained from the large scale stress field (Pollard et al., 2015), based on the horizontal divergence of the ice-shelf velocities and which is similar to parametrizations used elsewhere (Martin et al., 2011; Winkelmann et al., 2011; Levermann et al., 2012). Extensional stress is obtained via strain rate and the model SSA rheology. No distinction is made here between along-flow and transverse strains, whose combined effect is represented by ice divergence.

$$d_s = \frac{2}{\rho_i g} \left(\frac{\dot{\epsilon}}{A} \right)^{1/n} \quad (56)$$

$$d_b = \left(\frac{\rho_i}{\rho_w - \rho_i} \right) \frac{2}{\rho_i g} \left(\frac{\dot{\epsilon}}{A} \right)^{1/n} \quad (57)$$

where d_s and d_b are depths of dry-surface and basal crevasses respectively, and $\dot{\epsilon}$ is ice divergence. Calving is potentially applied to all points within the ice shelf, but the setting of divergence $\dot{\epsilon}$ depends on whether the floating ice covers all or a fraction of the cell area. A sub-grid parametrization of fractional ice area is used to set an adjusted ice thickness h and fractional cover f_i . At the ice-shelf edge adjacent to open ocean, the adjusted thickness h is the average of adjacent interior shelf thicknesses, each multiplied by a “downstream thinning” factor $1 - w[1 - \exp(\Delta x/100)]$, where the weight $w = \min[1, h_u/(h_a \exp(-\Delta x/100))]$, where Δx is the grid size in km, h_u is the unadjusted (grid-mean) ice thickness of the edge point, and h_a is the thickness of the adjacent interior point. The weight w is used to force $h \approx h_a$ for small amounts of ice ($h_u \ll h_a$), and to apply more downstream thinning when the edge cell has substantial ice cover. As in Pollard and DeConto (2012b), the fractional ice cover of the edge point is set to $f_i = h_u/h$, conserving ice mass.

For interior points (with $f_i = 1$), $\dot{\epsilon}$ in Eqs. (56–57) is set to the grid-scale divergence of ice velocity $\partial u/\partial x + \partial v/\partial y$. For edge points (with $f_i < 1$), it is set to the longitudinal spreading value for a freely floating unconfined ice face, using the adjusted ice thickness h as described above.

$$\dot{\epsilon} = \left(\frac{\partial u}{\partial x} + \frac{\partial v}{\partial y} \right) \quad \text{for} \quad f_i = 1 \quad (58)$$

$$\dot{\epsilon} = A \left(\frac{\rho_i g h}{4} \right)^n \quad \text{for} \quad f_i < 1 \quad (59)$$

An additional calving rate due to accumulated strain (valid for large ice shelves), is parametrized as

$$d_a = h \max[0, \ln(u/1600)] / \ln(1.2) \quad (60)$$

where h is ice thickness (adjusted as above if at the shelf edge) and u is local ice speed. d_a is zero for speeds up to 1600 m a^{-1} , and approaches h as speeds increase to $\sim 1900 \text{ m a}^{-1}$ and above, as they do in the outer regions of the Ross and Ronne shelves.

A pragmatic constraint is imposed for thin floating ice,

$$d_t = h \max[0, \min[1, (150 - h)/50]] \quad (61)$$

where again h is ice thickness (adjusted as above if at the shelf edge), and d_t is an additional crevasse depth. This simply has the effect of removing floating ice thinner than ~ 100 to 150 m , and reduces unrealistic areas of thin ice extending seaward of the modern Ross and Filchner–Ronne calving fronts, where they are not limited by Eq. (60). It has the side-effect of not allowing thin ice shelves to grow from small ($\sim 100 \text{ m}$) tidewater glaciers, which may be unrealistic in some cases but does not noticeably affect the large-scale modern and “retreat” simulations.

Surface crevasses containing water are deepened due to the additional opening stress of the liquid by an amount d_{wa} , where d_{wa} is (ρ_w/ρ_i) times the depth of water drained into the crevasse from mobile surface melt and/or rainfall. d_{wa} (m) is simply set to

$$d_{wa} = 100R^2 \quad (62)$$

where R is the annual surface melt plus rainfall available after refreezing in the surface mass balance scheme.

The overall calving rate C_r is expressed as a horizontal wastage rate (m a^{-1}):

$$C_r = 3000 \max[0, \min[1, (r - r_c)/(1 - r_c)]] \quad (63)$$

where r is the ratio of the combined crevasse depths to ice thickness $[d_s + d_b + d_a + d_t + d_{wa}]/h$, and r_c is a critical value for calving onset, set to 0.75 (Pollard et al., 2015).

Alternatively, the calving rate can also be defined as in Pollard and DeConto (2012b), i.e.,

$$C_r = 30(1 - w_c) + 3 \times 10^5 \max\left(\frac{\partial u}{\partial x} + \frac{\partial v}{\partial y}, 0\right) \frac{w_c h_e}{\Delta} \quad (64)$$

where $w_c = \min(1, h_e/200)$ is a weight factor and h_e is the subgrid ice thickness within a fraction of the ice edge grid cell that is occupied by ice (Pollard and DeConto, 2012a), defined by

$$h_e = \max\left[h_{\max} \times \max\left(0.25, e^{-h_{\max}/100}\right), 30, h\right] \quad (65)$$

where a minimum ice thickness of 30 m avoids too thin ice shelves. The value of h_{\max} is defined as the maximum ice thickness of the surrounding grid cells (grounded or floating) that are not adjacent to the ocean (Pollard and DeConto, 2012a). The calving rate C_r is then subtracted from the basal melt rate M in Eq. (7).

Given the relatively low spatial resolution of a large-scale ice-sheet model, small pinning points underneath ice shelves due to small bathymetric rises scraping the bottom of the ice and exerting an extra back pressure on the ice shelf (Berger et al., 2016; Favier et al., 2016)

are not taken into account. To overcome this a simple parametrization based on the standard deviation of observed bathymetry within each model cell was accounted for to introduce a given amount of basal friction of the ice shelf (Pollard and DeConto, 2012a). The fractional area f_g of ice in contact with sub-grid bathymetric high is defined as (modified from Pollard and DeConto, 2012a):

$$f_g = \max \left[0, 1 - \frac{h_w}{\sigma_b} \right] \quad (66)$$

where h_w is the thickness of the water column underneath the ice shelf and σ_b is the standard deviation of the bedrock variability (see above). This factor f_g is multiplied with β^2 in the basal friction. For the grounded ice sheet, $f_g = 1$; for the floating ice shelf in deeper waters, $f_g = 0$, so that the ice shelf does not experience any friction.

8.3 Control parameters for calving

ctr.calving :

- 0** : no calving, i.e., ice shelves will extend to the edge of the model domain (default)
- 1** : Apply ice front calving according to Pollard et al. (2015);
- 2** : Combination of calving=1 and calving=4 to make sure that ice shelves do not extend further than initially
- 3** : Apply ice front calving according to Pollard and DeConto (2012a);
- 4** : Calving front kept at observed position.
- 5** : Calving using LSF function (under development)

ctr.HydroFrac :

- 0** : no hydrofracturing (default)
- 1** : Apply hydrofracturing according to Pollard et al. (2015);

9 Glacial Isostatic Adjustment (GIA)

As a first approximation, the equilibrium vertical displacement of the lithosphere in response to an ice loading is described as the equilibrium vertical displacement of a horizontal linear elastic plate subject to a transverse load. In order to represent the viscous asthenosphere underneath the lithosphere, it is also assumed that this plate lies on a viscous substratum. This representation of the lithosphere is considered for instance in the commonly used elastic lithosphere–relaxing asthenosphere (ELRA) model in glaciology.

9.1 Bedrock deformation for a plate with constant thickness

Consider a thin rectangular plate with constant thickness h (and infinite horizontal dimension). The mechanical properties of the plate are given by its Young’s modulus E and its Poisson’s ratio ν (both properties are assumed to be constant). The plate is subjected to a transverse load q_b . Let w_b be the normal displacement of the plate (also called the deflection). For a thin rectangular plate, it is assumed that the shear strains ϵ_{xz} and ϵ_{xy} and the normal strain ϵ_{xx} is negligible, where we denoted the strain tensor by ϵ . In this context and using a Hooke’s law in linear elasticity (the plate is assumed to behave like a linear elastic material), the components σ_{xx} , σ_{yy} and σ_{xy} of the stress tensor are given by

$$\sigma_{xx} = \frac{E}{1 - \nu^2} (\epsilon_{xx} + \nu\epsilon_{yy}) \quad (67)$$

$$\sigma_{yy} = \frac{E}{1 - \nu^2} (\epsilon_{yy} + \nu\epsilon_{xx}) \quad (68)$$

$$\sigma_{xy} = \frac{1}{2}G\epsilon_{xy} \quad (69)$$

where $G = \frac{E}{2(1+\nu)}$ is the shear modulus. In the context of thin rectangular plates, these stress components can be written as:

$$\sigma_{xx} = -\frac{Ez}{1 - \nu^2} \left(\frac{\partial^2 w_b}{\partial x^2} + \nu \frac{\partial^2 w_b}{\partial y^2} \right) \quad (70)$$

$$\sigma_{yy} = -\frac{Ez}{1 - \nu^2} \left(\frac{\partial^2 w_b}{\partial y^2} + \nu \frac{\partial^2 w_b}{\partial x^2} \right) \quad (71)$$

$$\sigma_{xy} = -\frac{Ez}{1 + \nu} \frac{\partial^2 w_b}{\partial x \partial y} \quad (72)$$

where the vertical coordinate z is measured from the middle surface of the plate. The resulting twisting (or torsion) moments M_{xx} and M_{yy} and bending moment M_{xy} (equal to M_{yx}) are given by

$$M_{xx} = \int_{-h/2}^{h/2} \sigma_{xx} z dz = -D \left(\frac{\partial^2 w_b}{\partial x^2} + \nu \frac{\partial^2 w_b}{\partial y^2} \right) \quad (73)$$

$$M_{yy} = \int_{-h/2}^{h/2} \sigma_{yy} z dz = -D \left(\frac{\partial^2 w_b}{\partial y^2} + \nu \frac{\partial^2 w_b}{\partial x^2} \right) \quad (74)$$

$$M_{xy} = \int_{-h/2}^{h/2} \sigma_{xy} z dz = -D(1 - \nu) \frac{\partial^2 w_b}{\partial x \partial y} \quad (75)$$

where

$$D = \frac{Eh^3}{12(1 - \nu^2)} \quad (76)$$

is the flexural rigidity of the plate. Writing the equilibrium of forces and moments for the plate, it can be shown that the twisting and bending moments satisfy the following differential equation:

$$\frac{\partial^2 M_{xx}}{\partial x^2} + 2 \frac{\partial^2 M_{xy}}{\partial x \partial y} + \frac{\partial^2 M_{yy}}{\partial y^2} = -q_b \quad (77)$$

Substituting Eqs. (73)–(75) into Eq. (77) gives the following partial differential equation for the deflection w_b :

$$\begin{aligned} \frac{\partial^2}{\partial x^2} \left(-D \left(\frac{\partial^2 w_b}{\partial x^2} + \nu \frac{\partial^2 w_b}{\partial y^2} \right) \right) + 2 \frac{\partial^2}{\partial x \partial y} \left(-D(1 - \nu) \frac{\partial^2 w_b}{\partial x \partial y} \right) + \\ \frac{\partial^2}{\partial y^2} \left(-D \left(\frac{\partial^2 w_b}{\partial y^2} + \nu \frac{\partial^2 w_b}{\partial x^2} \right) \right) = -q_b \end{aligned} \quad (78)$$

or as D is assumed to be constant and ν is constant,

$$-D \left(\frac{\partial^4 w_b}{\partial x^4} + 2\nu \frac{\partial^4 w_b}{\partial x^2 \partial y^2} + \frac{\partial^4 w_b}{\partial y^4} \right) - 2D(1 - \nu) \frac{\partial^4 w_b}{\partial x^2 \partial y^2} = -q_b \quad (79)$$

that leads to

$$D \left(\frac{\partial^4 w_b}{\partial x^4} + 2 \frac{\partial^4 w_b}{\partial x^2 \partial y^2} + \frac{\partial^4 w_b}{\partial y^4} \right) \equiv D \nabla_x^4 w_b = q_b \quad (80)$$

9.2 Plate with constant thickness on a viscous substratum

We consider now that the plate lies on a viscous substratum with density ρ_b , which is the upper mantle density. In this case, we must account for the buoyancy force (which depends on the vertical displacement w_b) that the lithosphere experiences in the underlying viscous substratum. The buoyancy force acts to reduce the exerted force q_b by an amount $\rho_b g w_b$. Then, Eq. (80) writes in the presence of a viscous substratum as (Huybrechts and de Wolde, 1999; Pollard and DeConto, 2012a)

$$D \nabla_x^4 w_b + \rho_b g w_b = q_b \quad (81)$$

The load q_b is then defined by

$$q_b = \rho_i g h + \rho_s g h_w - \rho_i g h^{\text{eq}} - \rho_s g h_w^{\text{eq}}, \quad (82)$$

where h_w is the ocean column thickness, and h^{eq} and h_w^{eq} are the values of ice thickness and ocean column thickness in equilibrium, respectively, taken from modern observed

fields. Equation (81) is solved by a Green’s function (Huybrechts and de Wolde, 1999). The response to a point load P_b ($q_b \times \text{area}$) versus distance from the point load l is then given by

$$w_p(l) = \frac{P_b L_w^2}{2\pi D} \text{kei} \left(\frac{l}{L_w} \right), \quad (83)$$

where kei is a Kelvin function of zeroth order (defined as the imaginary part of a modified Bessel function of the second kind), and $L_w = (D/\rho_b g)^{1/4}$ is the flexural length scale. For any load, the different values of the point loads w_p are summed over all grid cells to yield $w_b(x, y)$.

9.3 Plate with spatially-varying thickness

Let us consider in this section a thin rectangular plate having a spatially-varying thickness $h(x)$. As previous, the plate is assumed to behave as a linear elastic material with constant Young’s modulus E and Poisson’s ratio ν . The plate is subjected to a transverse load q_b that induces a deflection w_b of the plate. We assume that the above thickness varies gradually and there is no abrupt variation in thickness so that the expressions for the bending and twisting moments derived earlier for plates of constant thickness (73)–(75) also apply with sufficient accuracy to the case of a thin rectangular having a spatially-varying thickness. Please note that in this case, the flexural rigidity D is therefore spatially varying, i.e.,

$$D = D(x) = \frac{Eh(x)^3}{12(1 - \nu^2)} \quad (84)$$

Substituting Eqs. (73)–(75) with the spatially-varying flexural rigidity $D(x)$ into Eq. (77) gives the following partial differential equation for the deflection w_b :

$$\begin{aligned} & D \nabla_x^4 w_b + 2 \frac{\partial D}{\partial x} \frac{\partial}{\partial x} (\nabla_x^2 w_b) + 2 \frac{\partial D}{\partial y} \frac{\partial}{\partial y} (\nabla_x^2 w_b) + \nabla_x^2 D (\nabla_x^2 w_b) \\ & - (1 - \nu) \left(\frac{\partial^2 D}{\partial x^2} \frac{\partial^2 w_b}{\partial y^2} - 2 \frac{\partial^2 D}{\partial x \partial y} \frac{\partial^2 w_b}{\partial x \partial y} + \frac{\partial^2 D}{\partial y^2} \frac{\partial^2 w_b}{\partial x^2} \right) + \rho_b g w_b = q_b \end{aligned} \quad (85)$$

In this case, Eq. (85) is solved using numerical methods instead of Green’s functions.

9.4 Time-dependent bedrock response

The actual rate of change in bedrock elevation is given by a simple relaxation scheme:

$$\frac{\partial b}{\partial t} = -\frac{1}{\tau_w} (b - b^{\text{eq}} + w_b), \quad (86)$$

where b is the actual bedrock elevation, b^{eq} is the elevation in equilibrium (taken from modern observed fields), and $\tau_w = 3000$ year (Pollard and DeConto, 2012a). Also here, we introduced spatially-varying values for τ_w , based on viscosity variations of the upper asthenosphere (Coulon et al., 2021).

9.5 Geoid changes

Mass changes and redistribution of mass at the surface of the Earth results in changes of the geoid height, hence differences in local sea level that may affect the exact position of the grounding determined from hydrostatic equilibrium. For a unit point mass, the perturbation in the geoid, apart from the deformation of the Earth, due to the point mass is

$$N(\theta) = \frac{a}{M_e} \left(\frac{1}{2 \sin(\theta/2)} \right) \quad (87)$$

where θ is the co-latitude of the load point. The angle θ represents the internal angle between the point mass and a given distance along the surface of the Earth with the Earth's centre. This function is then convoluted across the whole domain. Note that only the immediate change in ice volume in geoid height is considered, without taking into account the contribution of changes in the Earth's crust due to mass changes. This is because the geoid change is immediate, while isostatic changes are generally active on longer time scales. Furthermore, Earth rotational effects are neglected. The result influences the position of the grounding line and may retard grounding line retreat due to mass loss of ice sheets (Coulon et al., 2021).

9.6 Control parameters for GIA

ctr.BedAdj :

- 0** : no isostatic bedrock adjustment (default);
- 1** : isostatic adjustment of bedrock (with the modified ELRA model);
- 2** : local isostatic bed adjustment.

ctr.GeoidCalc :

- 0** : Local sea level changes not taken into account (default);
- 1** : Calculate height of the geoid (local sea level) compared to initial state, based on mass changes of the ice sheet.

10 Grounding-line flux condition for power-law sliding

10.1 Description

Previous studies have indicated that it is necessary to resolve the transition zone/boundary layer at sufficiently fine resolution in order to capture grounding-line migration accurately (Durand et al., 2009; Pattyn et al., 2012, 2013; Pattyn and Durand, 2013; Durand and Pattyn, 2015). In large-scale models, this can lead to unacceptably small time-steps and costly integrations. Pollard and DeConto (2009, 2012a) incorporated the boundary layer solution of Schoof (2007) directly in a numerical ice-sheet model at coarse grid resolution, so the flux, q_g , across model grounding lines is given by

$$q_g = \left[\frac{A(\rho_i g)^{n+1} (1 - \rho_i/\rho_s)^n A_b'^{1/m}}{4^n} \right]^{\frac{m}{m+1}} \Theta^{\frac{nm}{m+1}} h_g^{\frac{m(n+3)+1}{m+1}}. \quad (88)$$

This yields the vertically averaged velocity $u_g = q_g/h_g$ where h_g is the ice thickness at the grounding line. Θ in Eq. (88) accounts for back stress at the grounding line due to buttressing by pinning points or lateral shear, and is defined as

$$\Theta = \frac{b_f \tau_{xx} + (1 - b_f) \tau_f}{\tau_f}, \quad (89)$$

where τ_{xx} is the longitudinal stress just downstream of the grounding line, calculated from the viscosity and strains in a preliminary SSA solution without constraints given by Eq. (88), and τ_f the free-water tensile stress defined by

$$\tau_f = \frac{1}{2} \rho_i g h \left(1 - \frac{\rho_i}{\rho_s} \right). \quad (90)$$

The parameter b_f is an additional buttressing factor to control the buttressing strength of ice shelves and may be varied between 0 (no buttressing) and 1 (full buttressing). All experiments in this paper use $b_f = 1$, except the sensitivity experiments on ice-shelf de-buttressing where b_f is set to zero. Grounding-line ice thickness h_g is linearly interpolated in space by estimating the sub-grid position of the grounding line between the two surrounding floating and grounded h -grid points. Therefore, the height above floatation is linearly interpolated on the Arakawa C-grid between those two points to where it is zero. Subsequently, the bedrock elevation is linearly interpolated to that location, and the floatation thickness of ice for that bedrock elevation and current sea level is obtained (Pattyn et al., 2006; Gladstone et al., 2010; Pollard and DeConto, 2012a). The velocity u_g is then calculated at the grounding-line points and imposed as an internal boundary condition for the flow equations, hence overriding the large-scale velocity solution at the grounding line. $u_g = q_g/h_g$ is imposed exactly at the u -grid grounding line point when the flux q_g is greater than the large-scale sheet-shelf equation's flux at the grounding line.

Equation (88) applies equally to the y direction, with v_g and τ_{yy} instead of u_g and τ_{xx} . Note that spatial gradients of quantities parallel to the grounding line, which are not included in Schoof's flow-line derivation of Eq. (88), are neglected here (Katz and Worster, 2010; Gudmundsson et al., 2012; Pattyn et al., 2013). This parametrization was also found to yield results comparable to SSA models solving transient grounding line migration at high spatial

resolution of the order of hundreds of meters (Pattyn and Durand, 2013; Durand and Pattyn, 2015), despite the fact that Eq. (88) applies to steady-state conditions.

The use of the above-described flux condition has been analysed and criticised by Reese et al. (2018b), claiming non-physical behaviour of the buttressing factor in the flux condition. However, Reese et al. (2018b) only considered ice-sheet diagnostics, as negative values of buttressing vanish when the ice sheet is allowed to change over time. As a precaution, we limit anyway $0 \leq \Theta \leq 1$.

The ice sheet model f.ETISh also allows for modelling separate drainage basins at high resolution. In this case the SGL condition is not needed.

10.2 Control parameters for grounding-line flux

ctr.schoof :

- 0** : no grounding line flux correction (default);
- 1** : grounding line migration according to Schoof (2007);

11 Model initialization

11.1 Methodology

Model initialization can be done in different ways. One particular approach is to match the initial state of the ice sheet as close as possible to the observed one. Here we use this approach with the method from Pollard and DeConto (2012b) by optimizing basal sliding coefficients in an iterative fashion to allow for the ice thickness to match as closely the observed ice thickness. It is a two-step approach, where first the model is run forward in time using SIA without ice shelves (or grounding line flux condition), starting from modern observed bed and ice surface elevations and driven by the observed climatology (surface mass balance and temperature). Full thermomechanical coupling and temperature evolution, isostatic bedrock adjustment, and sub-grid ice-shelf pinning can equally be considered. Basal sliding coefficients $A_b(x, y)$ are initialized with a constant value (e.g., $A_b = 3 \times 10^{-9} \text{ m a}^{-1} \text{ Pa}^{-2}$ for the Antarctic ice sheet). This value is a nominal value for $m = 2$ and scaled for different values of m through a scaling factor that is multiplied with A_b

$$A_{\text{scale}} = 10^{5(2-m)} \quad (91)$$

At intervals of Δt_{inv} years, at each grounded ice grid point, the local basal sliding coefficients $A_b(x, y)$ in Eq. (40) are adjusted by a multiplicative factor (Pollard and DeConto, 2012b):

$$A_b^* = A_b \times 10^{\Delta z}, \quad (92)$$

for $\Delta z \leq \Delta z^0$. Δz is defined as

$$\Delta z = \max \left[-1.5, \min \left(1.5, \frac{h_s - h_s^{\text{obs}}}{h_s^{\text{inv}}} \right) \right], \quad (93)$$

and Δz^0 is its value from the previous iteration step, h_s^{obs} is the observed ice surface elevation and h_s^{inv} is a scaling constant. This means that the optimization of a local point is halted whenever its change Δz is larger than the one of the previous iteration step (Bernales et al., 2017). During the inversion procedure, basal temperature is still allowed to influence sliding. Adjusted $A_b^*(x, y)$ values are limited by defined limit values that take into account dependency on sliding law power coefficients m in Eq. (37). Values for A_b^* are only updated when $r > 0$ in Eq. (40), so that they are kept unchanged for ice temperatures below a certain limit.

In addition to Pollard and DeConto (2012b) we also introduce a regularization term that essentially smooths high-frequency noise in the basal sliding coefficients by using a Gaussian smoothing filter. The filter is only applied across the grounded domain with the exception of grid cells where the bedrock elevation is higher than 1000 m above present-day sea level and the roughness of the bedrock is above the 99% percentile of the total roughness of the domain. Contrary to Pollard and DeConto (2012b), the revised algorithm only requires about 50 000 years of forward integration to obtain an optimized friction field.

The second step consists of running the model with ice shelves (and grounding line flux condition if pertinent) using the HySSA velocity calculation. In addition to constraining the basal slip coefficients, melt/accretion rates under the floating ice shelves are updated using the method of Bernales et al. (2017).

11.2 Control parameters for optimization

ctr.inverse :

- 0** : normal forward model run (default);
- 1** : optimization of basal sliding coefficients A_s for the grounded ice sheet with fixed grounding line position.
- 2** : optimization of basal sliding coefficients A_s for the grounded ice sheet and sub-shelf melt/accretion for floating ice shelves. The parameter **ctr.GroundedMelt** defines whether MASKo or MASK is used for controlling the grounding line position.

ctr.Hinv : Scale factor on iterative optimization of ice thickness (Pollard and DeConto, 2012b). Default = 500.

ctr.Tinv : Time interval between updates in the optimization scheme (Pollard and DeConto, 2012b). Default = 200. For basin calculations, the value should be set lower (10 for instance) in order to reduce the run time.

ctr.HinvMelt : Scale factor on iterative optimization of ice thickness for ice shelves (Pollard and DeConto, 2012b). Default = 100.

ctr.TinvMelt : Time interval between updates in the optimization scheme (Pollard and DeConto, 2012b). Default = 50.

ctr.stopoptim : Fraction of total time at the end of the initialization run where updates of basal friction coefficients are not applied anymore (default=0.1)

ctr.GroundedMelt : Allow for the MASK to be defined by hydrostatic equilibrium in the optimization **ctr.inverse** = 2. Default=0.

12 Datasets for initialization and forcing

12.1 Datasets for the Antarctic ice sheet

For modelling the Antarctic ice sheet, the bedrock topography is either based on BedMachine Antarctica (Morlighem et al., 2019) or alternatively Bedmap2 (Fretwell et al., 2013), from which ice thickness, present-day surface topography and grounding-line position are derived. The data are also used to calculate the standard deviation of the bedrock topography σ_b . Since BedMachine provides a dataset at a high spatial resolution of 400 m, interpolation of data on a coarser grid requires a certain amount of smoothing. Best results are obtained by taking for ice thickness and bedrock elevation the mean value within a square representing the size of the final grid cell. After this smoothing, ice thickness and/or bedrock elevation is corrected to guarantee that grounded ice remains grounded and floating ice remains floated. In order to make sure that the grounding line cannot expend to the edge of the computational domain, bathymetry/bed topography is kept at -4000 m for two grid cells at the domain boundaries.

Surface mass balance and temperatures are obtained from Van Wessem et al. (2014), based on the output of the regional atmospheric climate model RACMO2 for the period 1979–2011 and evaluated using 3234 *in situ* mass balance observations and ice-balance velocities. For geothermal heat flux we employ either a recent update of Fox-Maule et al. (2005) due to Purucker (2013), based on low-resolution magnetic observations acquired by the CHAMP satellite between 2000 and 2010, the seismic-based heat flow dataset due to Shapiro and Ritzwoller (2004) or the more recent seismic-based dataset due to Lloyd et al. (2020).

13 Atmospheric forcing

Atmospheric forcing is applied either by reading air temperature and surface mass balance outputs from a climate model, either in a parameterized way, based on the observed fields of surface mass balance (defined as precipitation minus evapotranspiration minus runoff) and surface temperature.

When parameterized, for a change in background (forcing) temperature ΔT , corresponding fields of air temperature T_s , precipitation P are defined by (Huybrechts et al., 1998; Pollard and DeConto, 2012a)

$$T_s = T_s^{\text{obs}} - \gamma(h_s - h_s^{\text{obs}}) + \Delta T, \quad (94)$$

$$P = \dot{a}^{\text{obs}} \times 2^{(T_s - T_s^{\text{obs}})/\delta T}, \text{ or} \quad (95)$$

$$P = \dot{a}^{\text{obs}} \times (1 + 0.053(T_s - T_s^{\text{obs}})) \quad (96)$$

where $\gamma = 0.008^\circ\text{C m}^{-1}$ is the lapse rate and δT is 10°C (Pollard and DeConto, 2012a). The subscript ‘obs’ in Eq. (94) and Eq. (95) refers to the present-day observed value. Any forcing (increase) in background then leads to an overall increase in surface temperature corrected for elevation changes according to the environmental lapse rate γ . The second parametrization of P is due to Golledge et al. (2015), based on an analysis of CMIP5 models (Frieler et al., 2015). This leads to a smaller accumulation increase over the interior of ice sheets (and Antarctica in particular) with an increase in background temperature. The parametrizations of T_s and P can easily be replaced by values that stem from GCMs, with appropriate corrections for surface elevation (e.g., de Boer et al., 2015). If relevant, surface runoff fields (provided by an external climate model) can be corrected for changes in surface elevation with respect to the observed ice sheet geometry using the following correction (inferred from RCM outputs):

$$R_o = R_o^{\text{obs}} + 1.805 \left[\exp(0.5745 \times T_s) - \exp(0.5745 \times T_s^{\text{obs}}) \right] \quad (97)$$

Surface runoff, R_o , if not externally provided from a climate model, is parameterized using a positive degree-day model that calculates the yearly surface mass balance at the ice surface by capturing the basic physical processes of refreezing versus runoff in the snow column (Huybrechts and de Wolde, 1999), using the 2-m air temperature and the precipitation rate are used as inputs.

The positive degree-day model is a parameterization of surface melt where melt is assumed to be proportional to the number of positive degree-days (PDD), defined as the integral of positive Celsius temperature T over a time interval A , typically one year.

$$\text{PDD} = \int_0^A \max(T(t), 0) dt. \quad (98)$$

In order to account for sub-annual temperature variability around the freezing point (which significantly affects surface melt on a multi-year scale), it is common to assume a normal probability distribution of the surface air temperature T of known standard deviation σ_{PDD} around the daily temperature. It follows that number of PDDs can be computed using a double-integral formulation (Reeh, 1989)

$$\text{PDD} = \frac{1}{\sigma_{\text{PDD}}\sqrt{2\pi}} \int_0^A dt \int_{T_t}^{\infty} T \exp\left(-\frac{(T - T_M(t))^2}{2\sigma_{\text{PDD}}^2}\right) dT, \quad (99)$$

where T_M represents intra-annual variations of the daily air temperature, σ_{PDD} is taken as 4°C (Reeh, 1989). T_t is typically 0°C, though some studies have considered a positive temperature threshold different than 0°C (Golledge et al., 2019). This temperature integral is solved using the semi-analytical solution proposed by Calov and Greve (2005):

$$\begin{aligned} \text{PDD} = \int_0^A \left[\frac{\sigma_{\text{PDD}}}{\sqrt{2\pi}} \exp\left(-\frac{(T_t - T_M(t))^2}{2\sigma_{\text{PDD}}^2}\right) + \right. \\ \left. \frac{(T_M(t) - T_t)}{2} \text{erfc}\left(\frac{T_t - T_M(t)}{\sqrt{2}\sigma_{\text{PDD}}}\right) + T_t \right] dt \end{aligned} \quad (100)$$

where $\text{erfc}(x)$ is the complementary error function. The annual number of positive degree days represents a melt potential, used to melt snow and (superimposed) ice with degree-day factors of $s_f=0.003$ and $i_f=0.008$ m per degree day of water equivalent, respectively (Huybrechts and de Wolde, 1999). In order to approximate the amount of snow available for surface melting, the solid (snow, S_M) and liquid (rain, R_M) fraction of the total daily precipitation P_M , if not known, needs to be determined. This is typically done by determining a “rain fraction” factor R_f , with $R_M = P_M R_f$ and $S_M = P_M(1 - R_f)$.

Two distinct situations are allowed in order to define the intra-annual variations of the air temperature and precipitation rates.

1. The evolution of the monthly-mean (or sub-monthly) air temperatures and precipitation rates are known (ctr.monthly=1): they are therefore directly used as inputs to define the seasonal cycles of temperature and precipitation T_M and P_M .
2. The intra-annual variations of the air temperatures and precipitation rates are not known: T_M and P_M are therefore approximated based on the yearly-mean air temperature T_s and precipitation rate P . To do so, a sinusoidal seasonal cycle is added to T_s , using a peak-to-peak air amplitude T_a based on the ice elevation (and optionally the latitude). The precipitation rate is considered constant in time throughout the annual cycle, i.e. $P_M = P$.

Based on these seasonal variations, the model then computes the solid (snow) precipitation rate using the air temperature threshold with a linear transition: all precipitation during periods with air temperatures above $T_{\text{rain}} = 2^\circ\text{C}$ is interpreted as rain; all precipitation during periods with air temperatures below $T_{\text{snow}} = 0^\circ\text{C}$ is interpreted as snow. More specifically, the rain fraction R_f is computed as a function of the daily temperature above T_{snow} , with a statistic that is normally distributed and centered on the curve of the mean seasonal cycle T_M with a standard deviation σ_{RS} of 3.5°C, accounting for random temperature fluctuations and the daily cycle (Huybrechts and de Wolde, 1999):

$$R_f = 1 - \max\left[0, \min\left(\frac{T_{\text{rain}} - T_D}{T_{\text{rain}} - T_{\text{snow}}}, 1\right)\right], \quad (101)$$

where T_D is the semi-analytical solution of the temperature integral (Calov and Greve, 2005) above the T_{snow} threshold, used in order to take into account the daily variability of the temperature.

Using these intra-annual variations of the air temperature T_M , the snow accumulation rate (S_M) and the rainfall rate (R_M), the following algorithm is performed \sim every week (note that all quantities are expressed in ice equivalent):

1. The thickness of the snow pack is updated with the relevant snow accumulation rate. The seasonal cycles of zero-dimensional bulk quantities of snow and embedded melt-water are then run through several years to equilibrium, allowing to initialize the snow pack thickness, as the latter is carried over from year to year. Note that since we do not have a principled firn model, the snow depth is set to zero at the beginning of every new balance year.

$$h_{\text{snow}} = h_{\text{snow}} + S_M \quad (102)$$

2. The effective snow melt is calculated as follows. Note that it cannot exceed h_{snow} :

$$\text{ESM} = \min [\max (h_{\text{snow}}, 0), K_{\text{snow}} \text{PDD}] . \quad (103)$$

The remaining amount of PDD available after snow melt is calculated as

$$\text{PDD}_r = \max \left(\text{PDD} - \frac{\text{ESM}}{K_{\text{snow}}}, 0 \right) \quad (104)$$

3. The thickness of the snow pack is updated to account for the snow melt

$$h_{\text{snow}} = \max(h_{\text{snow}} - \text{ESM}, 0) \quad (105)$$

4. The effective ice melt EIM is ice is proportional the remaining amount of PDD,

$$\text{EIM} = K_{\text{ice}} \text{PDD}_r. \quad (106)$$

5. The weekly surface melt is the sum of ESM and EIM.

Net annual quantities are the integration of the weekly quantities across the seasonal cycle. At the end of the balance year, the total liquid water produced by the model (snow meltwater and rain) will refreeze in the snowpack and produce superimposed ice. Following Huybrechts and de Wolde (1999), the amount of refreezing depends on the cold content of the upper ice sheet layers, which puts an upper limit on the production of superimposed ice. The maximum amount of superimposed ice P_r , equivalent to the latent heat released to raise the temperature of the uppermost 5 m of the ice sheet surface to the melting point (where $L = 3.35 \times 10^5 \text{ J kg}^{-1}$ is the latent heat of fusion, $c_p = 2009 \text{ J kg}^{-1} \text{ }^\circ\text{C}^{-1}$ is the specific heat capacity of ice), is therefore calculated as

$$P_r = \frac{c_i}{L_f} d_{\text{ice}} |T_{\text{yr}}| \quad (107)$$

Any additional snow melt and/or rainfall is assumed to run off. As a physical mechanism can take place only to the extent that energy and mass are available in sufficient quantities, the effective refreezing E_r is the minimum of P_r and the total available water mass $W_r = \text{ESM} + R$ and is also limited by the annual precipitation P (Janssens and Huybrechts, 2000). The effective refreezing is calculated as follows

$$E_r = \min(P, \min(P_r, W_r)). \quad (108)$$

Note that the amount of refrozen rain (R_{ref}) that contributes to the production of superimposed ice (where $\text{ESM} < P_r$) is equivalent to $\max(P_r - \text{ESM}, 0)$.

As the surface of the previous year is considered impermeable, all ice meltwater is considered to run off. Total runoff is therefore

$$R_o = \text{EIM} + W_r - E_r. \quad (109)$$

Finally, the surface mass balance is then the sum of the different components, i.e., $\dot{a} = P - E_v - R_o$. Unless externally provided from climate model outputs, the evapotranspiration is assumed to remain constant.

Melting underneath the floating ice shelves is often based on parametrizations that relate sub-shelf melting to ocean temperature and ice-shelf depth (Beckmann and Goosse, 2003; Holland et al., 2008), either in a linear or a quadratic way (Martin et al., 2011; Pollard and DeConto, 2012a; de Boer et al., 2015; DeConto and Pollard, 2016). This leads to higher melt rates close to the grounding line, as the ice-shelf bottom is the lowest, i.e.,

$$M = \gamma_T \frac{\rho_s c_{po}}{L \rho_i} |T_{oc} - T_{fo}| (T_{oc} - T_{fo}), \quad (110)$$

and where M is the sub-ice-shelf basal melt rate, c_{po} is the specific heat capacity of the ocean, γ_T is the thermal exchange velocity, L is the latent heat of fusion, T_{oc} is the temperature of the ocean underneath the ice shelf, and T_{fo} is the freezing temperature defined by Beckmann and Goosse (2003) as:

$$T_{fo} = \lambda_1 S_o + \lambda_2 + \lambda_3 h_b, \quad (111)$$

where S_o is a value for the salinity of the ocean waters. We employ measurements of ocean temperature and salinity defined for each drainage basin of the Antarctic ice sheet based on Schmidtko et al. (2014) (see below for more details).

Alternatively, a linear version of Eq. (110) can be employed, which will also require a different value for γ_T . The latter is in general used as a general tuning parameter for the melt function (Favier et al., 2019).

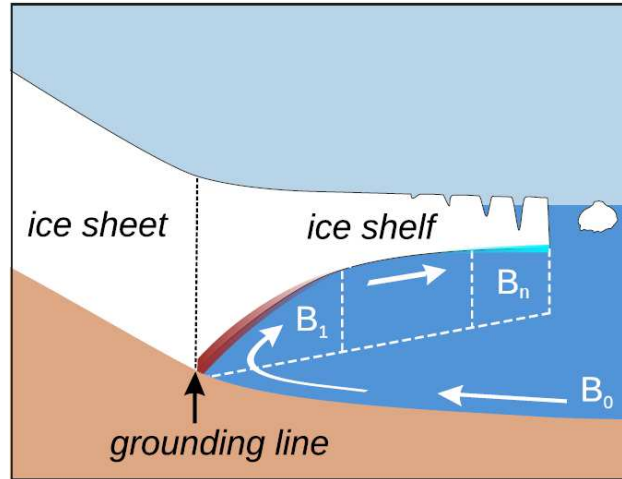


Figure 6: Schematic view of the PICO model. The model mimics the overturning circulation in ice shelf cavities: Ocean water from box B_0 enters the ice shelf cavity at the depth of the sea floor and is advected to the grounding line box B_1 . Freshwater influx from melting at the ice shelf base makes the water buoyant, causing it to rise. The cavity is divided into n boxes along the ice shelf base. Generally, the highest melt rates can be found near the grounding line, with lower melt rates or refreezing towards the calving front (Reese et al., 2018a).

14 Ocean forcing

14.1 The PICO ocean-coupler model

Alternatively to the sub-shelf melt parametrization, an ocean-coupling model has been implemented based on PICO (Potsdam Ice-shelf Cavity mOdel; Reese et al. (2018a)). PICO is developed from the ocean box model of Olbers and Hellmer (2010), which is designed to capture the basic overturning circulation in ice shelf cavities which is driven by the “ice pump” mechanism: melting at the ice shelf base near the grounding line reduces salinity and the ambient ocean water becomes buoyant, rising along the ice shelf base towards the calving front. Since the ocean temperatures on the Antarctic continental shelf are generally close to the local freezing point, density variations are primarily controlled by salinity changes. Melting at the ice-shelf base hence reduces the density of ambient water masses, resulting in a haline-driven circulation. Buoyant water rising along the shelf base draws in ocean water at depth, which flows across the continental shelf towards the deep grounding lines of the ice shelves. The warmer these water masses are, the stronger is the melting-induced ice pump. The Olbers and Hellmer (2010) box model describes the relevant physical processes and captures this vertical overturning circulation by defining consecutive boxes following the flow within the ice shelf cavity.

The strength of the overturning flux q is determined from the density difference between the incoming water masses on the continental shelf and the buoyant water masses near the deep grounding lines of the ice shelf. As PICO is implemented in an ice sheet model with characteristic time scales much slower than typical response times of the ocean, we assume steady-state ocean conditions and hence reduce the complexity of the governing equations of the Olbers and Hellmer (2010) model. We assume stable vertical stratification, which moti-

vates neglecting the diffusive heat and salt transport between boxes. Without diffusive transport between the boxes, some of the original ocean boxes from Olbers and Hellmer (2010) become passive and can be incorporated into the governing equations of the set of boxes used in PICO. We explicitly model a single open ocean box which provides the boundary conditions for the boxes adjacent to the ice shelf base following the overturning circulation, as shown in Fig. 6. In order to better resolve the complex melt patterns, PICO adapts the number of boxes based on the evolving geometry of the ice shelf. These simplifying assumptions allow us to analytically solve the system of governing equations (Reese et al., 2018a).

In general, PICO solves for the transport of heat and salt between boxes in contact with the base of the ice shelf, starting at the grounding line and ending at the ice front (boxes B_k for $k = \{1, \dots, n\}$, where n is typically less than or equal to 5). After simplification and assuming steady-state conditions, the balance of heat and salt in all boxes along the base of the ice shelf can be written as

$$\begin{aligned} q(T_{k-1} - T_k) - A_k m_k \frac{\rho_i}{\rho_s c_{po}} \frac{L}{\rho_s c_{po}} &= 0 \\ q(S_{k-1} - S_k) - A_k m_k S_k &= 0 \end{aligned} \quad (112)$$

Using a simplified formulation of the three-equation melt model by Holland and Jenkins (1999), the transport equations can be solved for salinity S_k and temperature T_k in box B_k and are dependent on the local pressure, the box area A_k , and the temperature T_{k-1} and salinity S_{k-1} of the upstream box $B - k - 1$. The strength of the overturning circulation, q , is calculated once per time step in box $B1$ from the density difference between the far-field and grounding line water masses:

$$q = C(\rho_0 - \rho_1) \quad (113)$$

The sub-shelf melt rate in each of the boxes is then determined as

$$m_k(x, y) = -\gamma_T \frac{\rho_s c_{po}}{L \rho_i} (\lambda_1 S_k(x, y) + \lambda_2 + \lambda_3 h_b(x, y) - T_k(x, y)) \quad (114)$$

where the subscript k refers to the values determined for each box within each ice shelf. Input data for the PICO model are present-day observed ocean temperature and salinity at depth on the continental shelf in front of contemporary ice shelves (Schmidtke et al., 2014). For the ice sheet to ‘feel’ these data, the ice sheet is divided up in different drainage basins based on the limits provided by NASA (Zwally, H. Jay, Mario B. Giovinetto, Matthew A. Beckley, and Jack L. Saba, 2012, [Antarctic and Greenland Drainage Systems](#), GSFC Cryospheric Sciences Laboratory). Mean values of ocean temperature and salinity in front of the ice shelves are then assigned to each basin, so that with retreat of the grounding line, individual ice shelves remain connected to the far-field ocean. These datasets are not calculated within f.ETISh, but should be provided. The PICO model automatically identifies individual ice shelves, divides them up in boxes and calculates ocean properties for each box. Sub-shelf melt rates within each box are determined using the local pressure of the overlying ice (Reese et al., 2018a).

14.2 PICOP and plume model

The plume model is a basal melt rate parametrization based on the theory of buoyant melt-water plumes that travel upward along the base of the ice shelf from the grounding line to the

location where the plume loses buoyancy. The two-dimensional formulation from Lazeroms et al. (2018) is adapted from the one-dimensional plume model developed by Jenkins (1991) for a plume travelling in direction X in an ocean with ambient temperature T_a and salinity S_a , either provided by PICO (which leads to the PICOP model) or from far-field ocean measurements (which is equivalent to the plume model). The method due to Pelle et al. (2019) has been employed. We begin by defining the grounding line depth, z_{gl} , over the entire ice shelf, as it is necessary to determine where individual plumes originate in order to employ this parametrization. As a first approximation, we solve an advection equation:

$$\begin{cases} v \cdot \nabla z_{gl} + \epsilon \Delta z_{gl} = 0 & \text{in } \Omega \\ z_{gl} = z_{gl0} & \text{on } \Gamma \end{cases} \quad (115)$$

where z_{gl0} is the grounding line height defined at the grounding line Γ , Ω is the ice shelf, and as a first approximation, v is the modelled, depth-averaged ice velocity. Note that ϵ is a small diffusion coefficient introduced to minimize noise and to provide numerical stability.

Once z_{gl} is defined, we continue by computing both the characteristic freezing point $T_{f,gl}$ and the effective heat exchange coefficient Γ_{TS} as follows:

$$T_{f,gl} = \lambda_1 S_a + \lambda_2 + \lambda_3 z_{gl} \quad (116)$$

$$\Gamma_{TS} = \Gamma_T \left(\gamma_1 + \gamma_2 \frac{T_a - T_{f,gl}}{\lambda_3} \times \frac{E_0 \sin \alpha}{C_d^{1/2} \Gamma_{TS_0} + E_0 \sin \alpha} \right) \quad (117)$$

A geometric scaling factor $g(\alpha)$ and length scale l are defined in order to give the plume model the proper geometry dependence and scaling according to the distance travelled along the plume path. The scaling factor and length scale are computed as follows:

$$g(\alpha) = \left(\frac{\sin \alpha}{C_d + E_0 \sin \alpha} \right)^{1/2} \left(\frac{C_d^{1/2} \Gamma_{TS}}{C_d^{1/2} \Gamma_{TS} + E_0 \sin \alpha} \right)^{1/2} \left(\frac{E_0 \sin \alpha}{C_d^{1/2} \Gamma_{TS} + E_0 \sin \alpha} \right) \quad (118)$$

$$\mu = \frac{T_a - T_{f,gl}}{\lambda_3} \times \frac{x_0 C_d^{1/2} \Gamma_{TS} + E_0 \sin \alpha}{x_0 (C_d^{1/2} \Gamma_{TS} + E_0 \sin \alpha)} \quad (119)$$

The dimensionless scale factor x_0 used in the second term of l defines the transition point between melting and refreezing and is constant for all model results. For a complete explanation of the individual terms that make up these two factors, see Sect. 2.2 of Lazeroms et al. (2018). The length scale is then used in the computation of the dimensionless coordinate, \hat{X} :

$$\hat{X} = \frac{z_b - z_{gl}}{l} \quad (120)$$

In order to ensure valid values of \hat{X} , we set a lower bound for the ambient ocean temperature: $T_a \geq \lambda_1 S_a + \lambda_2$. The melt rate \dot{m} is then calculated as

$$\dot{m} = \hat{M}(\hat{X}) \times M \quad (121)$$

where $\hat{M}(\hat{X})$ is a dimensionless melt curve defined in Lazeroms et al. (2018) and M is defined as

$$M = M_0 \times g(\alpha) \times (T_a - T_f(S_a, z_{gl}))^2 \quad (122)$$

14.3 Non-local melt-rate parametrization (ISMIP6)

Climate model projections have previously been used to compute ice-shelf basal melt rates in ice-sheet models, but the strategies employed –e.g. ocean input, parametrization, calibration technique, and corrections– have varied widely and are often ad-hoc. Jourdain et al. (2019) propose a methodology for the calculation of circum-Antarctic basal melt rates for floating ice, based on climate models, that is suitable for ISMIP6, the Ice Sheet Model Intercomparison Project for CMIP6 (6th Coupled Model Intercomparison Project). The past and future evolution of ocean temperature and salinity is derived from a climate model by estimating anomalies with respect to the modern day, which are added to an present-day climatology constructed from existing observational datasets. Temperature and salinity are extrapolated to any position potentially occupied by a simulated ice shelf. A simple formulation is proposed for a basal-melt parametrization in ISMIP6, constrained by the observed temperature climatology, with a quadratic dependency on either the non-local or local thermal forcing. Two calibration methods are proposed: (i) based on the mean Antarctic melt rate (MeanAnt) and (ii) based on melt rates near Pine Island’s deep grounding line (PIGL).

Melt rates in the common ISMIP6 experiments are derived using a slightly modified version of the non-local quadratic parametrization proposed by Favier et al. (2019). The parametrization is explicitly defined over regional sectors, rather than for a single ice shelf, and it includes a temperature correction:

$$m(x, y) = \gamma_0 \times \left(\frac{\rho_{sw} c_{pw}}{\rho_i L_f} \right)^2 \times (TF(x, y, z_{draft}) + \delta T_{sector}) \times |\langle TF \rangle_{draft \in sector} + \delta T_{sector}| \quad (123)$$

where $TF(x, y, z_{draft})$ is the thermal forcing at the ice-ocean interface, and $\langle TF \rangle_{draft \in sector}$ the thermal forcing averaged over all the ice-shelves of an entire sector. The uniform coefficient γ_0 , with units of velocity, is somewhat similar to the exchange velocity commonly used to calculate ice-ocean heat fluxes. The temperature correction δT_{sector} for each sector is needed to reproduce observation-based melt rates (at the scale of a sector) from observation-based thermal forcing.

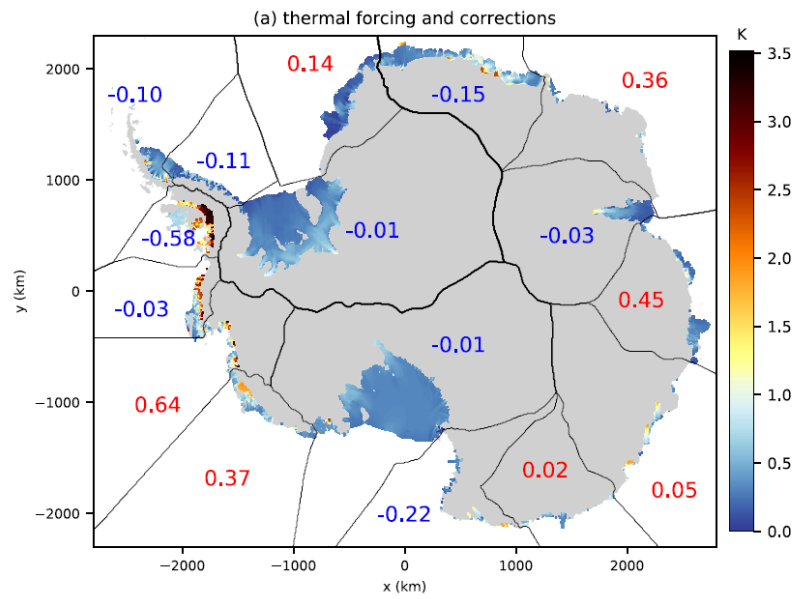


Figure 7: Thermal forcing (shaded) and its corrections (blue/red numbers indicating negative/positive δT) applied to each sector for non-local-MeanAnt with a slope dependency (Figure from Jourdain et al., 2019).

References

- Beckmann, A. and Goosse, H.: A parameterization of ice shelf-ocean interaction for climate models, *Ocean Modelling*, 5, 157 – 170, [https://doi.org/10.1016/S1463-5003\(02\)00019-7](https://doi.org/10.1016/S1463-5003(02)00019-7), 2003.
- Berger, S., Favier, L., Drews, R., Derwael, J.-J., and Pattyn, F.: The control of an uncharted pinning point on the flow of an Antarctic ice shelf, *Journal of Glaciology*, 62, 37–45, <https://doi.org/10.1017/jog.2016.7>, 2016.
- Bernales, J., Rogozhina, I., Greve, R., and Thomas, M.: Comparison of hybrid schemes for the combination of shallow approximations in numerical simulations of the Antarctic Ice Sheet, *The Cryosphere*, 11, 247–265, <https://doi.org/10.5194/tc-11-247-2017>, 2017.
- Bougamont, M., Christoffersen, P., Hubbard, A. L., Fitzpatrick, A. A., Doyle, S. H., and Carter, S. P.: Sensitive response of the Greenland Ice Sheet to surface melt drainage over a soft bed, *Nature Communications*, 5, 5052, <https://doi.org/10.1038/ncomms6052>, 2014.
- Bueler, E. and Brown, J.: Shallow shelf approximation as a “sliding law” in a thermomechanically coupled ice sheet model, *Journal of Geophysical Research: Earth Surface*, 114, <https://doi.org/10.1029/2008JF001179>, f03008, 2009.
- Bueler, E. and van Pelt, W.: Mass-conserving subglacial hydrology in the Parallel Ice Sheet Model version 0.6, *Geoscientific Model Development*, 8, 1613–1635, <https://doi.org/10.5194/gmd-8-1613-2015>, 2015.
- Bulthuis, K., Arnst, M., Sun, S., and Pattyn, F.: Uncertainty quantification of the multi-centennial response of the Antarctic ice sheet to climate change, *The Cryosphere*, 13, 1349–1380, <https://doi.org/10.5194/tc-13-1349-2019>, 2019.
- Calov, R. and Greve, R.: A semi-analytical solution for the positive degree-day model with stochastic temperature variations, *Journal of Glaciology*, 51, 2005.
- Coulon, V., Bulthuis, K., Whitehouse, P. L., Sun, S., Haubner, K., Zipf, L., and Pattyn, F.: Contrasting Response of West and East Antarctic Ice Sheets to Glacial Isostatic Adjustment, *Journal of Geophysical Research: Earth Surface*, 126, e2020JF006003, <https://doi.org/10.1029/2020JF006003>, e2020JF006003, 2021.
- de Boer, B., Dolan, A. M., Bernales, J., Gasson, E., Goelzer, H., Golledge, N. R., Sutter, J., Huybrechts, P., Lohmann, G., Rogozhina, I., Abe-Ouchi, A., Saito, F., and van de Wal, R. S. W.: Simulating the Antarctic ice sheet in the late-Pliocene warm period: PLISMIP-ANT, an ice-sheet model intercomparison project, *The Cryosphere*, 9, 881–903, <https://doi.org/10.5194/tc-9-881-2015>, 2015.
- DeConto, R. M. and Pollard, D.: Contribution of Antarctica to past and future sea-level rise, *Nature*, 531, 591–597, <https://doi.org/10.1038/nature17145>, 2016.
- Durand, G. and Pattyn, F.: Reducing uncertainties in projections of Antarctic ice mass loss, *The Cryosphere*, 9, 2043–2055, <https://doi.org/10.5194/tc-9-2043-2015>, 2015.

- Durand, G., Gagliardini, O., Zwinger, T., Le Meur, E., and Hindmarsh, R. C.: Full Stokes modeling of marine ice sheets: influence of the grid size, *Annals of Glaciology*, 50, 109–114, <https://doi.org/doi:10.3189/172756409789624283>, 2009.
- Edwards, T. L., Nowicki, S., Marzeion, B., Hock, R., Goelzer, H., Seroussi, H., Jourdain, N. C., Slater, D. A., Turner, F. E., Smith, C. J., McKenna, C. M., Simon, E., Abe-Ouchi, A., Gregory, J. M., Larour, E., Lipscomb, W. H., Payne, A. J., Shepherd, A., Agosta, C., Alexander, P., Albrecht, T., Anderson, B., Asay-Davis, X., Aschwanden, A., Barthel, A., Bliss, A., Calov, R., Chambers, C., Champollion, N., Choi, Y., Cullather, R., Cuzzone, J., Dumas, C., Felikson, D., Fettweis, X., Fujita, K., Galton-Fenzi, B. K., Gladstone, R., Golledge, N. R., Greve, R., Hattermann, T., Hoffman, M. J., Humbert, A., Huss, M., Huybrechts, P., Immerzeel, W., Kleiner, T., Kraaijenbrink, P., Le clec’h, S., Lee, V., Leguy, G. R., Little, C. M., Lowry, D. P., Malles, J.-H., Martin, D. F., Maussion, F., Morlighem, M., O’Neill, J. F., Nias, I., Pattyn, F., Pelle, T., Price, S. F., Quiquet, A., Radić, V., Reese, R., Rounce, D. R., Rückamp, M., Sakai, A., Shafer, C., Schlegel, N.-J., Shannon, S., Smith, R. S., Straneo, F., Sun, S., Tarasov, L., Trusel, L. D., Van Breedam, J., van de Wal, R., van den Broeke, M., Winkelmann, R., Zekollari, H., Zhao, C., Zhang, T., and Zwinger, T.: Projected land ice contributions to twenty-first-century sea level rise, *Nature*, 593, 74–82, <https://doi.org/10.1038/s41586-021-03302-y>, 2021.
- Favier, L., Pattyn, F., Berger, S., and Drews, R.: Dynamic influence of pinning points on marine ice-sheet stability: a numerical study in Dronning Maud Land, East Antarctica, *The Cryosphere*, 10, 2623–2635, <https://doi.org/10.5194/tc-10-2623-2016>, 2016.
- Favier, L., Jourdain, N. C., Jenkins, A., Merino, N., Durand, G., Gagliardini, O., Gillet-Chaulet, F., and Mathiot, P.: Assessment of sub-shelf melting parameterisations using the ocean–ice-sheet coupled model NEMO(v3.6)–Elmer/Ice(v8.3), *Geoscientific Model Development*, 12, 2255–2283, <https://doi.org/10.5194/gmd-12-2255-2019>, 2019.
- Flowers, G. E.: Modelling water flow under glaciers and ice sheets, *Proceedings of the Royal Society of London A: Mathematical, Physical and Engineering Sciences*, 471, <https://doi.org/10.1098/rspa.2014.0907>, 2015.
- Fox-Maule, C., Purucker, M. E., Olsen, N., and Mosegaard, K.: Heat Flux Anomalies in Antarctica Revealed by Satellite Magnetic Data, *Science*, 309, 464–467, 2005.
- Fretwell, P., Pritchard, H. D., Vaughan, D. G., Bamber, J. L., Barrand, N. E., Bell, R., Bianchi, C., Bingham, R. G., Blankenship, D. D., Casassa, G., Catania, G., Callens, D., Conway, H., Cook, A. J., Corr, H. F. J., Damaske, D., Damm, V., Ferraccioli, F., Forsberg, R., Fujita, S., Gim, Y., Gogineni, P., Griggs, J. A., Hindmarsh, R. C. A., Holmlund, P., Holt, J. W., Jacobel, R. W., Jenkins, A., Jokat, W., Jordan, T., King, E. C., Kohler, J., Krabill, W., Riger-Kusk, M., Langley, K. A., Leitchenkov, G., Leuschen, C., Luyendyk, B. P., Matsuoka, K., Mouginot, J., Nitsche, F. O., Nogi, Y., Nost, O. A., Popov, S. V., Rignot, E., Rippin, D. M., Rivera, A., Roberts, J., Ross, N., Siegert, M. J., Smith, A. M., Steinhage, D., Studinger, M., Sun, B., Tinto, B. K., Welch, B. C., Wilson, D., Young, D. A., Xiangbin, C., and Zirizzotti, A.: Bedmap2: improved ice bed, surface and thickness datasets for Antarctica, *The Cryosphere*, 7, 375–393, 2013.

- Frieler, K., Clark, P. U., He, F., Buizert, C., Reese, R., Ligtenberg, S. R. M., van den Broeke, M. R., Winkelmann, R., and Levermann, A.: Consistent evidence of increasing Antarctic accumulation with warming, *Nature Climate Change*, 5, 348 EP –, URL <https://doi.org/10.1038/nclimate2574>, 2015.
- Gagliardini, O., Cohen, D., Raback, P., and Zwinger, T.: Finite-element modeling of subglacial cavities and related friction law, *J. Geophys. Res.*, 112, n/a–n/a, <https://doi.org/10.1029/2006JF000576>, 2007.
- Gandy, N., Gregoire, L. J., Ely, J. C., Cornford, S. L., Clark, C. D., and Hodgson, D. M.: Exploring the ingredients required to successfully model the placement, generation, and evolution of ice streams in the British-Irish Ice Sheet, *Quaternary Science Reviews*, 223, 105 915, <https://doi.org/https://doi.org/10.1016/j.quascirev.2019.105915>, 2019.
- Gladstone, R. M., Payne, A. J., and Cornford, S. L.: Parameterising the Grounding Line in Ice Sheet Models, *The Cryosphere*, 4, 605–619, <https://doi.org/10.5194/tc-4-605-2010>, 2010.
- Goeller, S., Thoma, M., Grosfeld, K., and Miller, H.: A balanced water layer concept for subglacial hydrology in large-scale ice sheet models, *The Cryosphere*, 7, 1095–1106, <https://doi.org/10.5194/tc-7-1095-2013>, 2013.
- Golledge, N., Keller, E., Gomez, N., Naughten, K., Bernales, J., Trusel, L., and Edwards, T.: Global environmental consequences of twenty-first-century ice-sheet melt, *Nature*, 566, 65–72, 2019.
- Golledge, N. R., Kowalewski, D. E., Naish, T. R., Levy, R. H., Fogwill, C. J., and Gasson, E. G. W.: The multi-millennial Antarctic commitment to future sea-level rise, *Nature*, 526, 421–425, 2015.
- Gudmundsson, G. H., Krug, J., Durand, G., Favier, L., and Gagliardini, O.: The Stability of Grounding Lines on Retrograde Slopes, *The Cryosphere Discuss.*, 6, 2597–2619, <https://doi.org/10.5194/tcd-6-2597-2012>, 2012.
- Helanow, C., Iverson, N. R., Woodard, J. B., and Zoet, L. K.: A slip law for hard-bedded glaciers derived from observed bed topography, *Science Advances*, 7, <https://doi.org/10.1126/sciadv.abe7798>, 2021.
- Hindmarsh, R. C. A.: On the Numerical Computation of Temperature in an Ice Sheet, *J. Glaciol.*, 45, 568–574, 1999.
- Holland, D. M. and Jenkins, A.: Modeling Thermodynamic Ice-Ocean Interactions at the Base of an Ice Shelf, *J. Phys. Oceanogr.*, 29, 1787–1800, 1999.
- Holland, P. R., Jenkins, A., and Holland, D. M.: The response of ice shelf basal melting to variations in ocean temperature., *Journal of Climate*, 21, 2008.
- Hutter, K.: *Theoretical Glaciology*, Dordrecht, Kluwer Academic Publishers, 1983.
- Huybrechts, P.: The Antarctic Ice Sheet and Environmental Change: a Three-Dimensional Modelling Study, *Berichte für Polarforschung*, 99, 1–241, 1992.

- Huybrechts, P. and de Wolde, J.: The dynamic response of the Greenland and Antarctic ice sheets to multiple-century climatic warming, *Journal of Climate*, 12, 2169–2188, 1999.
- Huybrechts, P., Abe-Ouchi, A., Marsiat, I., Pattyn, F., Payne, A., Ritz, C., and Rommelaere, V.: Report of the Third EISMINT Workshop on Model Intercomparison, European Science Foundation (Strasbourg), 1998.
- Janssens, I. and Huybrechts, P.: The treatment of meltwater retention in mass-balance parameterisations of the Greenland ice sheet, *Annals of Glaciology*, 31, 133–140, 2000.
- Jenkins, A.: A one-dimensional model of ice shelf-ocean interaction, *Journal of Geophysical Research: Oceans*, 96, 20 671–20 677, <https://doi.org/10.1029/91JC01842>, 1991.
- Joughin, I., Smith, B. E., and Schoof, C. G.: Regularized Coulomb Friction Laws for Ice Sheet Sliding: Application to Pine Island Glacier, Antarctica, *Geophysical Research Letters*, 46, 4764–4771, <https://doi.org/https://doi.org/10.1029/2019GL082526>, 2019.
- Jourdain, N. C., Asay-Davis, X., Hattermann, T., Straneo, F., Seroussi, H., Little, C. M., and Nowicki, S.: A protocol for calculating basal melt rates in the ISMIP6 Antarctic ice sheet projections, *The Cryosphere Discussions*, 2019, 1–33, <https://doi.org/10.5194/tc-2019-277>, 2019.
- Katz, R. F. and Worster, M. G.: Stability of ice-sheet grounding lines, *Proceedings of the Royal Society of London A: Mathematical, Physical and Engineering Sciences*, pp. n/a–n/a, <https://doi.org/10.1098/rspa.2009.0434>, 2010.
- Lazeroms, W. M. J., Jenkins, A., Gudmundsson, G. H., and van de Wal, R. S. W.: Modelling present-day basal melt rates for Antarctic ice shelves using a parametrization of buoyant meltwater plumes, *The Cryosphere*, 12, 49–70, <https://doi.org/10.5194/tc-12-49-2018>, 2018.
- Le Brocq, A., Payne, A., Siegert, M., and Alley, R.: A subglacial water-flow model for West Antarctica, *Journal of Glaciology*, 55, 879–888, <https://doi.org/10.3189/002214309790152564>, 2009.
- Levermann, A., Albrecht, T., Winkelmann, R., Martin, M. A., Haseloff, M., and Joughin, I.: Kinematic first-order calving law implies potential for abrupt ice-shelf retreat, *The Cryosphere*, 6, 273–286, <https://doi.org/10.5194/tc-6-273-2012>, 2012.
- Liboutry, L.: A critical review of analytical approximate solutions for steady state velocities and temperatures in cold ice-sheets, *Zeitschrift für Gletscherkunde und Glazialgeologie*, 35, 135–148, 1979.
- Lloyd, A. J., Wiens, D. A., Zhu, H., Tromp, J., Nyblade, A. A., Aster, R. C., Hansen, S. E., Dalziel, I. W. D., Wilson, T., Ivins, E. R., and O’Donnell, J. P.: Seismic Structure of the Antarctic Upper Mantle Imaged with Adjoint Tomography, *Journal of Geophysical Research: Solid Earth*, 125, <https://doi.org/https://doi.org/10.1029/2019JB017823>, 2020.
- Lüthi, M., Funk, M., Iken, A., Gogineni, S., and Truffer, M.: Mechanisms of fast flow in Jakobshavn Isbræ, West Greenland: Part III. Measurements of ice deformation, temperature and cross-borehole conductivity in boreholes to the bedrock, *Journal of Glaciology*, 48, 369–385, <https://doi.org/10.3189/172756502781831322>, 2002.

- Ma, Y., Gagliardini, O., Ritz, C., Gillet-Chaulet, F., Durand, G., and Montagnat, M.: Enhancement factors for grounded ice and ice shelves inferred from an anisotropic ice-flow model, *Journal of Glaciology*, 56, 805–812, <https://doi.org/10.3189/002214310794457209>, 2010.
- MacAyeal, D. R.: Large-scale Ice Flow over a Viscous Basal Sediment: Theory and Application to Ice Stream B, Antarctica, *J. Geophys. Res.*, 94, 4071–4087, 1989.
- Martin, M. A., Winkelmann, R., Haseloff, M., Albrecht, T., Bueler, E., Khroulev, C., and Levermann, A.: The Potsdam Parallel Ice Sheet Model (PISM-PIK) Part 2: Dynamic equilibrium simulation of the Antarctic ice sheet, *The Cryosphere*, 5, 727–740, <https://doi.org/10.5194/tc-5-727-2011>, 2011.
- Morland, L.: Unconfined Ice-Shelf Flow, in: *Dynamics of the West Antarctica Ice Sheet*, edited by van der Veen, C. J. and Oerlemans, J., pp. 99–116, Kluwer Acad., Dordrecht, Netherlands, 1987.
- Morlighem, M., Rignot, E., Binder, T., Blankenship, D., Drews, R., Eagles, G., Eisen, O., Ferraccioli, F., Forsberg, R., Fretwell, P., Goel, V., Greenbaum, J. S., Gudmundsson, H., Guo, J., Helm, V., Hofstede, C., Howat, I., Humbert, A., Jokat, W., Karlsson, N. B., Lee, W. S., Matsuoka, K., Millan, R., Mouginot, J., Paden, J., Pattyn, F., Roberts, J., Rosier, S., Ruppel, A., Seroussi, H., Smith, E. C., Steinhage, D., Sun, B., Broeke, M. R. v. d., Ommen, T. D. v., Wessem, M. v., and Young, D. A.: Deep glacial troughs and stabilizing ridges unveiled beneath the margins of the Antarctic ice sheet, *Nature Geoscience*, <https://doi.org/10.1038/s41561-019-0510-8>, 2019.
- Olbers, D. and Hellmer, H.: A box model of circulation and melting in ice shelf caverns, *Ocean Dynamics*, 60, 141–153, <https://doi.org/10.1007/s10236-009-0252-z>, 2010.
- Pattyn, F.: Antarctic Subglacial Conditions inferred from a Hybrid Ice Sheet/Ice Stream Model, *Earth Planet. Sci. Lett.*, 295, 451–461, 2010.
- Pattyn, F.: Sea-level response to melting of Antarctic ice shelves on multi-centennial timescales with the fast Elementary Thermomechanical Ice Sheet model (f.ETISh v1.0), *The Cryosphere*, 11, 1851–1878, <https://doi.org/10.5194/tc-11-1851-2017>, 2017.
- Pattyn, F. and Durand, G.: Why marine ice sheet model predictions may diverge in estimating future sea level rise, *Geophysical Research Letters*, 40, 4316–4320, <https://doi.org/10.1002/grl.50824>, 2013.
- Pattyn, F., De Brabander, S., and Huyghe, A.: Basal and Thermal Control Mechanisms of the Ragnhild Glaciers, East Antarctica, *Ann. Glaciol.*, 40, 225–231, 2005.
- Pattyn, F., Huyghe, A., De Brabander, S., and De Smedt, B.: Role of transition zones in marine ice sheet dynamics, *Journal of Geophysical Research: Earth Surface*, 111, n/a–n/a, <https://doi.org/10.1029/2005JF000394>, f02004, 2006.
- Pattyn, F., Schoof, C., Perichon, L., Hindmarsh, R. C. A., Bueler, E., de Fleurian, B., Durand, G., Gagliardini, O., Gladstone, R., Goldberg, D., Gudmundsson, G. H., Huybrechts, P., Lee, V., Nick, F. M., Payne, A. J., Pollard, D., Rybak, O., Saito, F., and Vieli, A.: Results

- of the Marine Ice Sheet Model Intercomparison Project, MISIMIP, *The Cryosphere*, 6, 573–588, <https://doi.org/10.5194/tc-6-573-2012>, 2012.
- Pattyn, F., Perichon, L., Durand, G., Favier, L., Gagliardini, O., Hindmarsh, R. C., Zwinger, T., Albrecht, T., Cornford, S., Docquier, D., Fürst, J. J., Goldberg, D., Gudmundsson, G. H., Humbert, A., Hütten, M., Huybrechts, P., Jouvet, G., Kleiner, T., Larour, E., Martin, D., Morlighem, M., Payne, A. J., Pollard, D., Rückamp, M., Rybak, O., Seroussi, H., Thoma, M., and Wilkens, N.: Grounding-line migration in plan-view marine ice-sheet models: results of the ice2sea MISIMIP3d intercomparison, *Journal of Glaciology*, 59, 410–422, <https://doi.org/10.3189/2013JoG12J129>, 2013.
- Pelle, T., Morlighem, M., and Bondzio, J. H.: Brief communication: PICOP, a new ocean melt parameterization under ice shelves combining PICO and a plume model, *The Cryosphere*, 13, 1043–1049, <https://doi.org/10.5194/tc-13-1043-2019>, 2019.
- Pelletier, C., Fichefet, T., Goosse, H., Haubner, K., Helsen, S., Huot, P.-V., Kittel, C., Klein, F., Le clec’h, S., van Lipzig, N. P. M., Marchi, S., Massonnet, F., Mathiot, P., Moravveji, E., Moreno-Chamarro, E., Ortega, P., Pattyn, F., Souverijns, N., Van Achter, G., Van den Broucke, S., Vanhulle, A., Verfaillie, D., and Zipf, L.: PARASO, a circum-Antarctic fully-coupled ice-sheet - ocean - sea-ice - atmosphere - land model involving f.ETISH1.7, NEMO3.6, LIM3.6, COSMO5.0 and CLM4.5, *Geoscientific Model Development Discussions*, 2021, 1–59, <https://doi.org/10.5194/gmd-2021-315>, 2021.
- Pollard, D. and DeConto, R. M.: Modelling West Antarctic Ice Sheet Growth and Collapse Through the Past Five Million Years, *Nature*, 458, 329–332, <https://doi.org/10.1038/nature07809>, 2009.
- Pollard, D. and DeConto, R. M.: Description of a Hybrid Ice Sheet-Shelf Model, and Application to Antarctica, *Geosci. Model Dev.*, 5, 1273–1295, <https://doi.org/10.5194/gmd-5-1273-2012>, 2012a.
- Pollard, D. and DeConto, R. M.: A simple inverse method for the distribution of basal sliding coefficients under ice sheets, applied to Antarctica, *The Cryosphere*, 6, 953–971, <https://doi.org/10.5194/tc-6-953-2012>, 2012b.
- Pollard, D., DeConto, R. M., and Alley, R. B.: Potential Antarctic Ice Sheet retreat driven by hydrofracturing and ice cliff failure, *Earth and Planetary Science Letters*, 412, 112 – 121, 2015.
- Purucker, M.: Geothermal heat flux data set based on low resolution observations collected by the CHAMP satellite between 2000 and 2010, and produced from the MF-6 model following the technique described in Fox Maule et al. (2005), <http://websrv.cs.umn.edu/isis/index.php>, 2013.
- Reeh, N.: Parameterization of melt rate and surface temperature on the Greenland ice sheet, *Polarforschung*, 59, 113–128, 1989.
- Reese, R., Albrecht, T., Mengel, M., Asay-Davis, X., and Winkelmann, R.: Antarctic sub-shelf melt rates via PICO, *The Cryosphere*, 12, 1969–1985, <https://doi.org/10.5194/tc-12-1969-2018>, 2018a.

- Reese, R., Winkelmann, R., and Gudmundsson, G. H.: Grounding-line flux formula applied as a flux condition in numerical simulations fails for buttressed Antarctic ice streams, *The Cryosphere*, 12, 3229–3242, <https://doi.org/10.5194/tc-12-3229-2018>, 2018b.
- Ritz, C.: Time Dependent Boundary Conditions for Calculation of Temperature Fields in Ice Sheets, *IAHS Publ.*, 170, 207–216, 1987.
- Ritz, C.: Un Modèle Thermo-Mécanique d’Evolution pour le Bassin Glaciaire Antarctique Vostok-Glacier Byrd: Sensibilité aux Valeurs des Paramètres Mal Connus, PhD Thesis, Univ. J. Fourier, 1992.
- Schmidtko, S., Heywood, K. J., Thompson, A. F., and Aoki, S.: Multidecadal warming of Antarctic waters, *Science*, 346, 1227–1231, <https://doi.org/10.1126/science.1256117>, 2014.
- Schoof, C.: The effect of cavitation on glacier sliding, *Proc. R. Soc. Lond. A*, 461, 609–627, <https://doi.org/10.1098/rspa.2004.1350>, 2005.
- Schoof, C.: Ice sheet grounding line dynamics: Steady states, stability, and hysteresis, *Journal of Geophysical Research: Earth Surface*, 112, n/a–n/a, <https://doi.org/10.1029/2006JF000664>, f03S28, 2007.
- Seroussi, H., Nowicki, S., Payne, A. J., Goelzer, H., Lipscomb, W. H., Abe-Ouchi, A., Agosta, C., Albrecht, T., Asay-Davis, X., Barthel, A., Calov, R., Cullather, R., Dumas, C., Galton-Fenzi, B. K., Gladstone, R., Golledge, N. R., Gregory, J. M., Greve, R., Hattermann, T., Hoffman, M. J., Humbert, A., Huybrechts, P., Jourdain, N. C., Kleiner, T., Larour, E., Leguy, G. R., Lowry, D. P., Little, C. M., Morlighem, M., Pattyn, F., Pelle, T., Price, S. F., Quiquet, A., Reese, R., Schlegel, N.-J., Shepherd, A., Simon, E., Smith, R. S., Straneo, F., Sun, S., Trusel, L. D., Van Breedam, J., van de Wal, R. S. W., Winkelmann, R., Zhao, C., Zhang, T., and Zwinger, T.: ISMIP6 Antarctica: a multi-model ensemble of the Antarctic ice sheet evolution over the 21st century, *The Cryosphere*, 14, 3033–3070, <https://doi.org/10.5194/tc-14-3033-2020>, 2020.
- Shapiro, N. M. and Ritzwoller, M. H.: Inferring Surface Heat Flux Distributions Guided by a Global Seismic Model: Particular Application to Antarctica, *Earth and Planetary Science Letters*, 223, 213–224, 2004.
- Stokes, G.: On the theories of internal friction of fluids in motion, *Trans. Cambridge Philos. Soc.*, 8, 287–305, 1845.
- Sun, S., Cornford, S. L., Moore, J. C., Gladstone, R., and Zhao, L.: Ice shelf fracture parameterization in an ice sheet model, *The Cryosphere*, 11, 2543–2554, <https://doi.org/10.5194/tc-11-2543-2017>, 2017.
- Tsai, V. C., Stewart, A. L., and Thompson, A. F.: Marine ice-sheet profiles and stability under Coulomb basal conditions, *Journal of Glaciology*, 61, 205–215, <https://doi.org/doi:10.3189/2015JoG14J221>, 2015.
- van der Wel, N., Christoffersen, P., and Bougamont, M.: The influence of subglacial hydrology on the flow of Kamb Ice Stream, West Antarctica, *Journal of Geophysical Research: Earth Surface*, 118, 97–110, <https://doi.org/10.1029/2012JF002570>, 2013.

- Van Pelt, W. J. and Oerlemans, J.: Numerical simulations of cyclic behaviour in the Parallel Ice Sheet Model (PISM), *Journal of Glaciology*, 58, 347–360, <https://doi.org/10.3189/2012JoG11J217>, 2012.
- Van Wessem, J., Reijmer, C., Morlighem, M., Mouginot, J., Rignot, E., Medley, B., Joughin, I., Wouters, B., Depoorter, M., Bamber, J., Lenaerts, J., De Van Berg, W., Van Den Broeke, M., and Van Meijgaard, E.: Improved representation of East Antarctic surface mass balance in a regional atmospheric climate model, *Journal of Glaciology*, 60, 761–770, <https://doi.org/doi:10.3189/2014JoG14J051>, 2014.
- Weertman, J.: Effect of a Basal Water Layer on the Dimensions of Ice Sheets, *Journal of Glaciology*, 6, 191–207, <https://doi.org/10.3189/S0022143000019213>, 1966.
- Winkelmann, R., Martin, M. A., Haseloff, M., Albrecht, T., Bueler, E., Khroulev, C., and Levermann, A.: The Potsdam Parallel Ice Sheet Model (PISM-PIK) Part 1: Model description, *The Cryosphere*, 5, 715–726, 2011.
- Zoet, L. K. and Iverson, N. R.: A slip law for glaciers on deformable beds, *Science*, 368, 76–78, <https://doi.org/10.1126/science.aaz1183>, 2020.